Modification and Characterisation of Zeolite Beta as a Possible Basic Catalyst for Biodiesel Production

Marta Gomes Figueira de Almeida Bordonhos

Thesis to obtain the Master of Science Degree in

Chemical Engineering

Supervisors: Prof. Dr Carlos Manuel Faria de Barros Henriques
Dr Vladimir L. Zholobenko

Examination Committee

Chairperson:	Prof. Dr Sebastião Manuel Tavares da Silva Alves
Supervisor:	Prof. Dr Carlos Manuel Faria de Barros Henriques
Member of the Committee:	Prof. Dr José Manuel Félix Madeira Lopes

December 2016

ACKNOWLEDGEMENTS

I would first like to express my deepest gratitude to Dr Vladimir Zholobenko for all his support, availability, dedication, teachings and patience (and chocolate!) since day one of my stay at Keele. I would also like to express my sincere gratitude to Prof. Carlos Henriques for all his help, guidance and valued suggestions throughout all these months.

I would like to thank everyone at the Birchall Centre for their friendliness, and for always making me feel welcome. An earnest thank you goes out to Dr Richard Darton for his availability and precious help in time of need. I also want to single out Aqeel and Cátia for all their support and good times, especially Cátia, my fellow countrywoman, who has made everything so much easier just by being there, always available, always ready to help, always up for a quick chat. Words cannot describe how grateful I am that you were there. Having someone that I could relate to and with whom I could freely speak my mother tongue has made my stay at Keele feel more like home. My day-to-day would not have been the same otherwise.

I want to thank my hallmates for all their help and friendship, especially Nam, my “partner in crime”, for all the geek outs, talks and long walks into town.

I also want to thank my friends, for holding the other end of a 1700 km long tether back home in Lisbon and for always being there.

Last, but definitely not least, I want to thank my family, particularly my parents, for providing me with this opportunity, for always supporting me and never giving up on me. For all their love and chastisements. For the daily chats and the tighter hugs.

I want to dedicate this work to my Grandmother Helena, a woman of science whom I have always looked up to, who instilled in me the love for science, and for all her love, until the very last…

Isto é para si…

ABSTRACT

The ever growing worldwide consumption of energy, associated with non-renewable fossil fuels, has led to an increasing interest in the field of renewable energy sources such as biodiesel.

Biodiesel is most commonly produced by the transesterification of animal fats or vegetable oils. Basic zeolites appear to be a good choice as heterogeneous catalysts for this process, due to their highly porous structure and reusability.

The acid form of zeolite beta (BEA-150, $SiO_2/Al_2O_3 = 300$) was subject to modification techniques in order to increase its basicity, by substituting its native H^+ with K^+. Seven samples were prepared: three by wet impregnation (KNO_3, K/Al = 1; KOH, K/Al = 2, 10) and four by ion exchange (KNO_3, K/Al = 1, 10; KOH, K/Al = 2, 10). The eight (original and modified) samples were calcined at 500 °C for 4 hours.

The following characterisation techniques have been used: SEM/EDS, XRD, FTIR and N_2 sorption experiments. In FTIR, pyridine was used to probe the acidity of the eight uncalcined samples, and acetylene for the basicity of the eight calcined samples. In N_2 sorption experiments, MultiPoint BET and *t*-plot method were used to determine total and external and micropore surface areas; pore size distribution and diameter were determined by DFT.

Results have shown that samples treated with a 10-fold molar excess of KOH have suffered severe structural damage caused by desilication and dealumination.

SEM/EDS has shown a particle size of approximately 1 μm, although this may correspond to agglomerates of smaller particles. XRD patterns have shown that the samples are composed of around 50 – 60% of polymorph B. FTIR has detected a small amount of strong BAS and LAS. Increased basic character has been detected by redshifts in acetylene post-adsorption spectra. Excluding destroyed samples, the average values (for the remaining 12 samples) of MultiPoint BET surface area, *t*-plot method micropore volume and DFT pore diameter were, respectively, 512 m^2/g, 0.113 cm^3/g and 9.2 Å.

Keywords: zeolite, BEA-150, characterisation, modification, catalyst, biodiesel

RESUMO

O aumento do consumo energético global, maioritariamente associado a combustíveis fósseis, tem levado a um crescente interesse no campo das fontes de energia renováveis, tal como o biodiesel.

O biodiesel é geralmente produzido através da transesterificação de gorduras animais ou óleos vegetais. Zeólitos básicos apresentam-se como uma boa opção como catalisadores heterogéneos para este processo, devido à sua estrutura altamente porosa e possibilidade de reutilização.

Foram utilizadas técnicas de modificação na forma ácida do zeólito beta (BEA-150, $SiO_2/Al_2O_3 = 300$) com o objectivo de aumentar a sua basicidade, através da substituição do seu catião extra-rede nativo, H^+, por K^+. Foram preparadas sete amostras: três por impregnação (KNO_3, K/Al = 1, 10; KOH, K/Al = 2, 10) e quatro por permuta iónica (KNO_3, K/Al = 1, 10; KOH, K/Al = 2, 10). As oito amostras (original e modificadas) foram calcinadas a 500 °C durante 4 horas.

As técnicas de caracterização usadas foram: SEM/EDS, XRD, FTIR e experiências de sorção de N_2. Na técnica de FTIR, a acidez das oito amostras não calcinadas foi testada com piridina e a basicidade das oito amostras calcinadas com acetileno. Nas experiências de sorção de N_2, os métodos de MultiPoint BET e *t*-plot foram utilizados para determinar as áreas superficiais totais e externa e microporosa; a distribuição de tamanhos e diâmetro dos poros foram determinados por DFT.

Os resultados mostraram que as amostras tratadas com um excesso molar de 10 de KOH apresentam danos estruturais severos, causados por dessilicação e desaluminação.

Através de SEM/EDS foi determinado um tamanho de partícula de aproximadamente 1 μm, que pode, no entanto, corresponder a aglomerados de partículas mais pequenas. Os padrões de XRD mostraram que as amostras são compostas por cerca de 50 – 60% de polimorfo B. Nas análises de FTIR foi detectada uma pequena quantidade de BAS e LAS fortes. O aumento do carácter básico foi detectado por *redshifts* nos espectros de pós-adsorção de acetileno. Excluindo as amostras destruídas, os valores médios (para as restantes 12 amostras) da área superficial de MultiPoint BET, volume microporoso calculado pelo método *t*-plot e diâmetro do poro obtido por DFT foram, respectivamente, 512 m^2/g, 0,113 cm^3/g e 9,2 Å.

Palavras-chave: zeólito, BEA-150, caracterização, modificação, catalisador, biodiesel

TABLE OF CONTENTS

LIST OF TABLES

LIST OF FIGURES

NOMENCLATURE

- a.u. – Arbitrary units
- AAS – Atomic absorption spectroscopy
- BAS – Brønsted acid site(s)
- BEA, β – Zeolite beta
- BET – Brunauer-Emmett-Teller
- CBU – Composite building unit(s)
- cf. – *confer*
- DFT – Density functional theory
- e.g. – *exempli gratia*
- EDS – Energy-dispersive X-ray spectroscopy
- EFAL – Extra-framework aluminium
- ETS-10 – Engelhard titanosilicate structure 10
- FAAE – Fatty acid alkyl ester(s)
- FAU – Faujasite
- FFA – Free fatty acid(s)
- FTIR – Fourier transform infrared
- i.e. – *id est*
- ICP – Induced coupled plasma
- IE – Ion exchange
- IM – Iminium
- IR – Infrared
- IUPAC – International Union of Pure and Applied Chemistry
- IZA – International Zeolite Association
- LAS – Lewis acid site(s)
- MAS – Magic angle spinning
- NMR – Nuclear magnetic resonance
- PBU – Primary building unit(s)
- Py – Pyridine
- RT – Room temperature
- SBU – Secondary building unit(s)
- SEM – Scanning electron microscopy
- SIMS – Secondary ion mass spectroscopy
- TAG – Triacylglycerol(s)
- TGA – Thermogravimetric analysis
- TPD – Temperature programmed desorption
- WI – Wet impregnation
- XPS – X-ray photoelectron spectroscopy
- XRD – X-ray diffraction
- Al_2O_3 – Aluminium oxide
- AlOH – EFAL hydroxyl group
- C_2H_2 – Acetylene
- CaO – Calcium oxide
- CH_3ONa – Sodium methoxide
- H_2SO_4 – Sulfuric acid
- HCl – Hydrochloric acid
- HNO_3 – Nitric acid
- KNO_3 – Potassium nitrate
- KOH – Potassium hydroxide
- MgO – Magnesium oxide
- NaOH – Sodium hydroxide
- SiO_2 – Silicon dioxide
- SiOH – Silanol group
- TiO_2 – Titanium dioxide
- ZrO_2 – Zirconium dioxide

1. INTRODUCTION

In a world reliant on non-renewable fossil fuels as a means to obtain energy, biodiesel production is becoming an ever more viable, reliable and ecological alternative [1].

Biodiesel is the designation given to the renewable fuel that originates from the conversion of lipid feedstocks rich in triacylglycerols (TAG), such as animal fats or vegetable oils, into fatty acid alkyl esters (FAAE). The production of biodiesel can be achieved through a number of different processes although the most commonly used is the catalysed alcoholysis of the lipid feedstocks into FAAE and glycerol, known as transesterification. In this reaction, one molecule of TAG reacts with three molecules of the chosen alcohol, typically methanol or ethanol, to generate one molecule of glycerol and three molecules of FAAE, as shown step-by-step in Figure 1 [1].

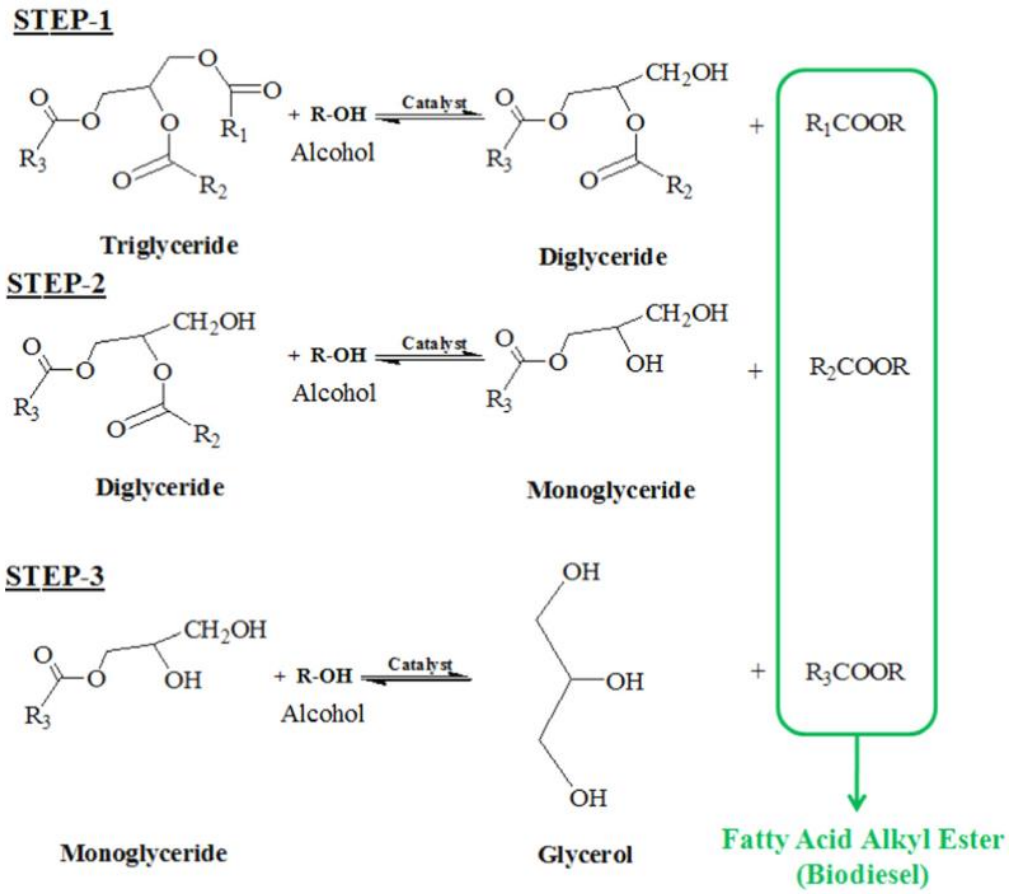

Figure 1 – Stepwise transesterification of TAG into FAAE (biodiesel) [1]

With a more pronounced incidence in low-grade oils, free fatty acids (FFA) are one of the major impurities found in lipid feedstocks. FFA can also undergo an alcoholysis reaction commonly known as esterification, as shown in Figure 2 [2], and although they can be converted into biodiesel, their presence in the lipid feedstock, associated with a high water content, can affect the transesterification process, particularly in the separation of glycerol and FAAE during the purification phase, due to the possibility of the formation of soaps [3].

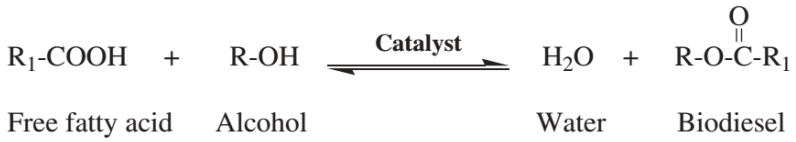

Figure 2 – Esterification of FFA into biodiesel [2]

Amidst the catalysts available to be used in the alcoholysis process, two major groups can be identified: homogeneous and heterogeneous. Inside these two groups the catalysts can be classified as acidic, basic or a combination of the previous two, i.e., bi-functional [1]. Table 1 summarises the principal characteristics of these types of catalysts.

Table 1 – Different types of catalysts used in biodiesel production [1] [2] [3]

	Homogeneous	**Heterogeneous**
Acid	• Transesterification and esterification reactions can occur simultaneously and at mild reaction conditions • Insensitive to FFA content in the lipid feedstock • Slow reaction rate • Separation from product is difficult • Corrosive nature of some catalysts can lead to corrosion problems on the reactor and pipelines • E.g.: H_2SO_4, HCl, HNO_3	• Transesterification and esterification reactions can occur simultaneously • Insensitive to FFA content in the lipid feedstock • Easy separation from product and possibility of regeneration and reuse • Severe reaction conditions • Possibility of product contamination due catalyst leaching • E.g.: ZrO_2, TiO_2, cation-exchanged resins, zeolites
Base	• Fastest reaction rate (up to 4000 faster than acid catalysed reaction) • Mild reaction conditions • Low cost and wide availability of catalysts • Sensitive to FFA content in the lipid feedstock • Possibility of soap formation • Product purification generates significant amounts of wastewater • E.g.: NaOH, KOH, CH_3ONa	• Faster reaction rate than acid catalysed reaction • Mild reaction conditions • Easy separation from product and possibility of regeneration and reuse • Low cost and wide availability of catalysts • Sensitive to FFA content in the lipid feedstock • Possibility of soap formation and product contamination due catalyst leaching • E.g.: MgO, CaO, anion-exchanged resins, zeolites
Acid-Base, Bi-functional	• Two-step alcoholysis reaction, in which acid catalyst is used first to promote FFA esterification, followed by base-catalysed TAG transesterification • Large quantities of catalysts required • Separation from and purification of product is difficult • E.g.: H_2SO_4 followed by KOH	• Two-step alcoholysis reaction possible with a combination of two different catalysts • Use of single bi-functional catalyst eliminates the need of the two-step process, reducing overall costs • Easy separation from product and possibility of regeneration and reuse • E.g.: Quintine-3T, zeolites

Of the catalysts mentioned in Table 1, zeolites are the most versatile, due to their modifiable chemical composition and pore size distribution [4]. The acid-base properties and shape selectivity of these molecular sieves can be adjusted via modification techniques, such as wet impregnation, ion exchange or calcination. For biodiesel production, heterogeneous catalysts are usually preferred, with the basic types being favoured over the acid types, due to the former's more advantageous characteristics.

In addition to being used as catalysts, zeolites are also widely used as adsorbents and in the composition of detergents. Their relative low price, accessibility, reusability and low toxicity have contributed to a growing market trend for zeolites, which is expected to keep rising until 2020, as shown in Figure 3 [5].

Figure 3 – Global zeolite market projection for the years 2014 – 2020 [5]

Zeolites are the focus of this thesis. The main goal of this work was to obtain a highly porous, basic zeolite by using the modification techniques of wet impregnation and ion exchange, followed by calcination, and to perform a thorough characterisation of the original and modified samples, by using different characterisation methods, such as SEM/EDS, XRD, IR and N_2 sorption experiments. The zeolite used was zeolite beta (BEA, β), obtained in its protonic form from *Zeolyst International*, with a SiO_2/Al_2O_3 molar ratio of 300 (Si/Al = 150).

Following this introduction, chapter 2 presents a literature review on zeolites. Chapter 3 describes the procedures and techniques used, with the subsequent results featured and discussed in chapter 4. To finalise, chapter 5 presents the main conclusions of this work and suggestions for future work.

This work was developed in the Birchall Centre, located in the Lennard-Jones Laboratories, at Keele University, Staffordshire, United Kingdom.

2. ZEOLITES

Zeolites are crystalline aluminosilicate porous materials that have an infinite three-dimensional framework structure. The first zeolite, stilbite, was discovered in 1756 by Swedish mineralogist Axel Cronstedt, who then derived the name “zeolite” from the two Greek terms for “to boil”, *zeo*, and “stone”, *lithos* [6].

The zeolite structure is composed of TO_4 tetrahedra that are connected by the sharing of oxygen atoms and where T represents a silicon (Si) or aluminium (Al) atom [6] with $Si/Al \geq 1$, in accordance with the Loewestein rule [7]. SiO_4 tetrahedra are neutrally charged unlike AlO_4 tetrahedra, which have a net negative charge of (-1). This net negative charge is countered by loosely-held extra-framework cations of hydrogen or of alkali or alkali-earth metals, such as sodium, potassium, magnesium or calcium [6]. The linking of the TO_4 tetrahedra originates channels and cavities of molecular dimensions in the zeolite structure that are occupied by the cations and water molecules, and constitute the zeolite’s pores [6].

There are two types of zeolites: natural and synthetic. Natural zeolites originate from basaltic and volcanic rock and are formed by the reaction of solid aluminosilicates with mineralising aqueous solutions, under a typical pH of approximately 10, temperatures below 100 °C, and over a period of thousands of years [6]. Synthetic zeolites, first synthesised in 1948 by New Zealander chemist Richard Barrer, can be the artificial counterparts of natural zeolites, and are essentially prepared by mixing a Si source, an Al source, an alkali cation organic template, a mineraliser agent and a solvent to form a gel, that will then crystallise under the required pH and temperature conditions [6]. According to the International Zeolite Association (IZA), and as of September of 2016, there have been identified 232 different zeolite framework types[1], of which 67 correspond to natural zeolites [8] [9].

2.1. STRUCTURE

The structural formula of zeolites, based on the crystallographic unit cell, is given by:

$$M_{x/n}[(AlO_2)_x(SiO_2)_y]\cdot wH_2O$$

where M is the extra-framework cation, n is that cation’s valence, x and y are the total number of tetrahedra per unit cell (typically $1 \leq y/x \leq 5$) and w is the number of water molecules per unit cell [6].

As mentioned above, the TO_4 tetrahedra are linked to each other by the sharing of oxygen atoms. Each TO_4 unit is called a primary building unit (PBU). The joining of two PBU originates a secondary building unit (SBU) that connects to other SBU, for a finite or infinite (e.g.: chains, layers) number of times in the configuration of polygons or simple polyhedra, generating composite building units (CBU), that usually constitute the cages within the structure. The assembly of SBU and CBU gives rise to the three-dimensional framework structure of the zeolite. A simplified schematic of this construction scheme is shown in Figure 4 [10]. To differentiate between zeolite framework types, IZA has developed a three

[1] Framework types describe the connection of the framework’s tetrahedrally coordinated T-atoms in their highest possible symmetry and not other parameters (e.g.: composition, unit cell size) [6]. As such, chemically different materials can have the same framework type, as is the case of natural zeolite faujasite and its synthetic counterparts, zeolites X and Y.

letter code, typically derived from the name of the original zeolitic material: for example *BEA corresponds to the structure of zeolite beta and FAU corresponds to the structures of faujasite and zeolites X and Y [11]. The *Atlas of Zeolite Framework Types* [12], published on behalf of IZA, provides a detailed compilation of framework types, SBU, CBU and other pertinent information.

The pores created in the zeolite structure by the linked TO_4 tetrahedra are defined by the number of T atoms in their openings. Considering the pore opening size, the majority of zeolites can be classified as [11]:

- Small-pored zeolites – pore openings of 8 T atoms, with a free diameter of 0.30 – 0.45 nm;
- Medium-pored zeolites – pore openings of 10 T atoms, with a free diameter of 0.45 – 0.60 nm;
- Large-pored zeolites – pore openings of 12 T atoms, with a free diameter of 0.60 – 0.80 nm.

As a consequence of synthesis conditions or post-synthesis modifications, the crystalline structure of zeolites can be affected by the appearance of faults or defects, and, in some cases, be completely destroyed.

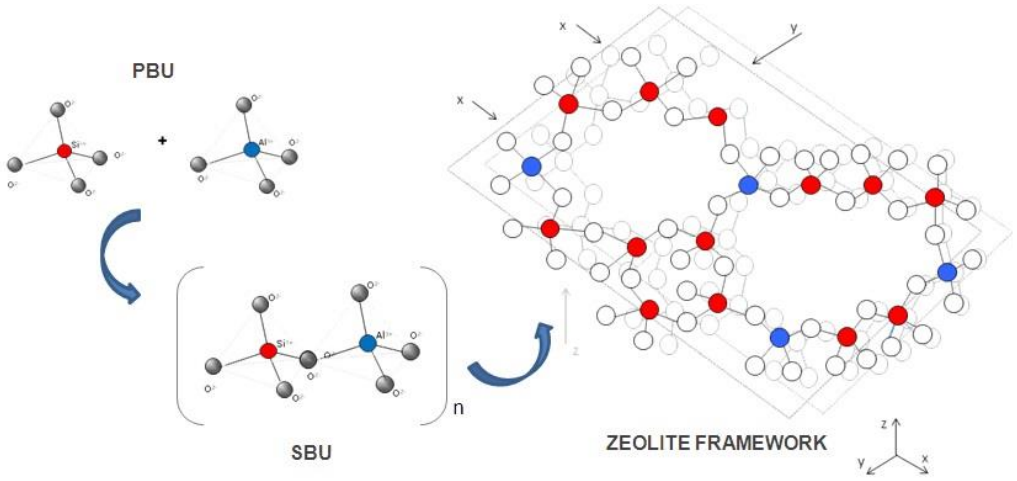

Figure 4 – Simplified assembly of a zeolite framework structure (adapted from [10])

2.2. PROPERTIES

Zeolites have found widespread application as catalysts in the fine chemicals (e.g.: MTBE cracking, cyclohexene hydration), petrochemical (e.g.: aromatisation, MTO conversion) and oil refining (e.g.: Fluid Catalytic Cracking, hydrocracking) industries [11], owing to their versatile properties and cost/effect value. Their high thermal and hydrothermal stability allows them to be used as catalysts under severe temperature conditions. Their microporous structure of channels and cavities provides an expansive internal surface area, in which there is a high concentration of active sites, whose strength and number can be altered to suit the experimental conditions, and also shape selectivity, which allows preferential reaction pathways to be carried out by the effects of reactant/product size exclusion or transition state selectivity [13]. The ion exchange properties of zeolites are ideal for detergents and water treatment and their adsorbent qualities, in addition to their shape selectivity and uniform pore size, allow zeolites to be used as molecular sieves and filters.

2.3. ACIDITY

The concept of acidity can be understood through different perspectives. Brønsted and Lowry proposed that an acid is a substance that can donate protons (H^+), while Lewis' proposal stated that an acid is a substance that can accept electron pairs.

In addition to the properties mentioned above, the acidic nature of zeolites is what makes them the most widely used and characterised solid acid catalysts [14]. The acidity of zeolites is translated into the form of two types of acid sites: Brønsted (BAS) and Lewis acid sites (LAS).

Brønsted acid sites, the most important catalytic centres in acid catalysis on zeolites, can typically be found inside the zeolites' pores and consist of bridging hydroxyl (OH) groups, Si-O(H)-Al, formed by the bonding of a proton to a framework oxygen (O) atom connecting two tetrahedrally coordinated Si to Al atoms [14] [15], as it is shown in Figure 5. Considering that the presence of protons (and any extra-framework cation) is a consequence of the overall negative charge of AlO_4 tetrahedra, it can be said that the maximum number of protonic acid sites equals the number of framework Al atoms. In reality, however, the number of protonic sites may be inferior to the number of framework Al atoms as a result of incomplete cation exchange or dihydroxylation and dealumination phenomena [11].

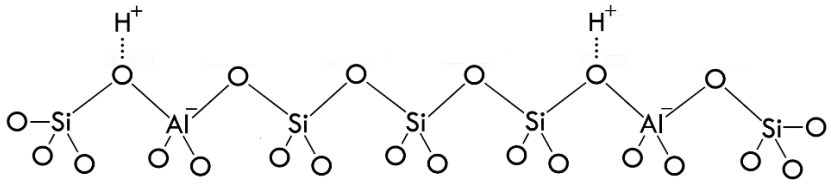

Figure 5 – Brønsted acid sites in zeolites

The activity of protonic groups is directly proportional to their strength, but also depends on their accessibility in terms of location and reagent molecule size, and proximity [11]. There are, however, other parameters that influence the activity, and therefore strength, of acid sites. One such parameter is the angle of T-O-T bonds: the greater this angle is, the higher the acid strength will be [11] [15]. The substitution of Al with other trivalent atoms also affects the acidity of the group as follows [11] [15]:

$$\text{Si-O(H)-B} < \text{Si-O(H)-In} << \text{Si-O(H)-Fe} < \text{Si-O(H)-Ga} < \text{Si-O(H)-Al}$$

As stated above, the number of extra-framework protons (or cations) is, in theory, equal to the number of framework Al atoms and, as such, it is trivial to conclude that the number of protonic groups increases with increasing Al content (or decreasing Si/Al ratio) [6]. As the number of protonic groups increases, however, the strength of each individual group decreases, and that is due to Al being less electronegative than Si [6] [11]. This electronegativity difference causes a higher electron transfer from O to Si (than from O to Al), and, consequently, from O to H and, as such, the O-H bond will have a higher ionic character, i.e., the O-H bond will be stronger [11]. O-H bond strength, therefore, also affects acid strength: a stronger O-H bond will have less tendency to break, i.e., to "let go" of its H, making the group less acidic (as per the definition of Brønsted acid sites).

Bridging OH groups are not the only hydroxyl groups found in zeolites. Other hydroxyl groups such as silanol (SiOH) groups, that stem from framework defects or crystal termination, and extra-framework

aluminium (EFAL) hydroxyl groups (AlOH), that originate from dealumination phenomena, can also contribute, albeit in a lesser degree, to the overall acidity of the zeolite [11] [15].

Lewis acid sites, although not as active as catalytic sites as protonic sites, can increase the acidic strength of their neighbouring Brønsted acid sites, by attracting electron density from BAS, which will lower their O-H bond strength, thus making these neighbouring BAS stronger [11] [16]. Electron acceptors by nature, the majority of LAS in zeolites originate from EFAL, which are the outcome of dealumination caused by mild steaming or calcination, and Al structural defects, caused by dihydroxylation of BAS as a consequence of dehydration of the structure at high temperatures [14]. LAS can also be attributed to charge-balancing extra-framework alkali cations and heteroatoms substituted at framework T positions [17].

2.4. BASICITY

Basicity in zeolites is an overall less industrially applied concept than acidity, and therefore a much less studied subject, however no less important, particularly in the scope of this work.

While Lewis and Brønsted acid sites have different definitions, Lewis and Brønsted basic sites are effectively the same, as a lone electron pair donor is also a proton acceptor [17]. In zeolites, most basic sites are associated with framework oxygen atoms due to their negative charge, that is a consequence of the presence of framework Al [17]. As such, the higher the framework Al content, i.e. the lower the Si/Al ratio is, the more basic centres the zeolite will have, and the more basic it will be, considering that Al has a lower electronegativity than Si [16].

The negative charge on framework oxygen atoms is dependent on the chemical composition of the zeolite (i.e. Si/Al ratio and type of extra-framework cation) [17]. To compare them, Mortier applied Sanderson's electronegativity equalization principle to zeolites [16] [17] [18]. It has been theorised that "the average partial charge of the framework oxygen atoms is proportional to the difference between the intermediate electronegativity of the zeolite atoms and of oxygen" [17]. As such, the lower the electronegativity of the extra-framework cation is, the lower the intermediate electronegativity will be, and as a result, the framework oxygen atoms will be more negative, i.e., more basic [17] [18]. For zeolites with exchanged alkali cations, the order of basicity is as follows [16] [17] [18]:

$$Li < Na < K < Rb < Cs$$

The zeolite's structure also influences the negative charge on the framework oxygen atoms. As opposed to what happens with the acidic strength, decreasing the T-O-T bonding angle or increasing its binding length improves the zeolite's basicity [19].

Framework oxygen atoms are not the only basic centres found in zeolites. Other examples include hydroxy groups that originate from water dissociation in hydrated extra-framework cations and basic oxygen atoms or hydroxy groups in oxide clusters [17].

2.5. CHARACTERISATION

Over the years several characterisation techniques have been developed and improved to shed light on both chemical and physical properties of materials. When it comes to zeolites, as mentioned before, the catalytic potential of these aluminosilicates will be defined by properties such as [11]:

- Zeolite structure and crystallinity;
- Global chemical and unit cell compositions;
- Size and shape of crystallites;
- Textural properties;
- Nature, location, concentration and strength of active sites.

The following table summarises some of the available techniques suited for the characterisation of the different zeolite properties [11] [16].

Table 2 – Characterisation techniques used to assess zeolite properties [11] [16]

Property	Characterisation Technique
Structure (Crystallinity)	X-Ray Diffraction (XRD)
Chemical Composition	Atomic Absorption Spectroscopy (AAS) Induced Coupled Plasma (ICP)
Superficial Composition	X-Ray Photoelectron Spectroscopy (XPS) Secondary Ion Mass Spectroscopy (SIMS)
Framework Composition	^{29}Si, ^{27}Al Magic-Angle Spinning – Nuclear Magnetic Resonance (MAS-NMR) XRD
Morphology	Scanning Electron Microscopy (SEM)
Texture	Physical Adsorption (e.g.: N_2)
Acidity	BAS, LAS Fourier Transform Infrared (FTIR) Temperature Programmed Desorption (TPD) Test model reactions Calorimetry
Basicity	OH FTIR TPD Test model reactions

2.6. ZEOLITE BETA

Zeolite beta was first synthesised in 1967 [20], and its framework structure fully determined twenty-one years later, in 1988 [21] [22]. This zeolite has a 12-membered ring system of mutually intersecting three-dimensional channels, a high thermal stability, Si/Al ratios that can go from 10 to more than 100, and it is usually in the form of small crystallites in the range of 20 – 50 nm [23] [24].

It is generally accepted that zeolite beta is a randomly ordered structure of two intergrown polymorphs, A and B [6] [22]. Polymorph A presents an ABAB(…) stacking sequence, whereas polymorph B presents an ABCA(…) stacking sequence, as can be seen in Figure 6 [25]. Because of its

disordered structural nature, IZA has added an asterisk to the code given to zeolite beta, *BEA, which was assigned in 1992 [26].

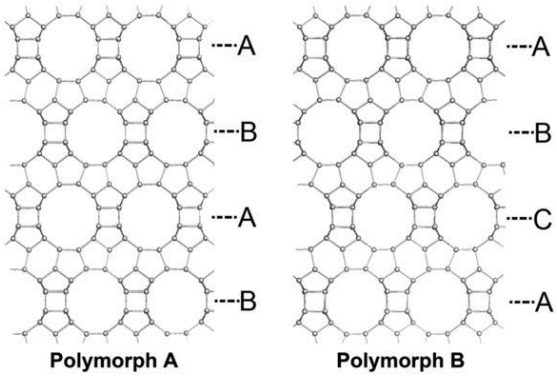

Figure 6 – Stacking order of polymorphs A and B of zeolite beta [25]

Zeolite beta's disordered structure and small crystallite size render it a highly active catalyst [22] [24]. While a and b directions have unhindered channels, the channels in direction c are affected by the faulting caused by the stacking of the different polymorphs, and as a result exhibit an increased tortuosity [22], as it shown below in Figure 7 [26]. The a and b directions' linear channels have pore openings of 7.5×5.7 Å, whereas the c direction's tortuous channels have pore openings of 6.5×5.6 Å [21].

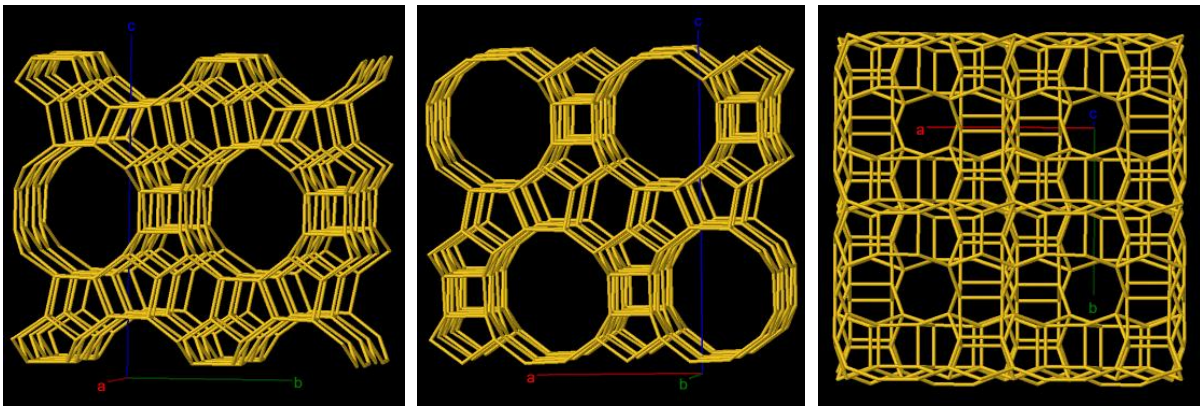

Figure 7 – Channel system in zeolite beta along a, b and c directions [26]

As mentioned above, due to its unusual configuration and general small crystallite size, zeolite beta is a good catalyst, and as such has been used in a number of hydrocarbon-related processes, such as: *i*-butane/butane alkylation, cumene production via benzene alkylation with propene, cracking, hydroisomerisation and dewaxing of petroleum oils and organic synthesis [11] [23] [27]. Low Al, alkali ion-exchanged zeolites have been used in biodiesel production [28]. If the zeolite has big crystallites, steric and diffusion limitations can occur, particularly if the molecules have large dimensions [29]. This problem can be attenuated by reducing crystallite size and generating mesopores within the zeolite structure, therefore creating hierarchical zeolites [29].

The zeolite beta used in this work has a Si/Al ratio of 150 (BEA-150) and has been acquired from *Zeolyst International* (reference CP811C-300) in its protonic form. Because it is in its protonic form and because of its low Al content it has an overall acidic nature.

3. EXPERIMENTAL TECHNIQUES

3.1. MODIFICATION TECHNIQUES

As mentioned in the previous chapter, zeolite BEA-150 has an acidic nature due to being in its protonic form and due to its low aluminium content. To obtain a basic zeolite, potassium cations were introduced to substitute the native protons via the two following chemical treatments with aqueous solutions of KNO_3 or KOH, in varying K/Al ratios (1, 2 and 10). KNO_3 was obtained in powder form from *Alfa Aesar*, with an assay of 99% and KOH was obtained in pellet form from *Fisher Chemical*, with an assay of 86.15%. The two following chemical treatments were used:

WET IMPREGNATION

In wet impregnation (WI), a small volume of solution containing the precursor is added to the support, under stirring conditions, followed by drying [30]. Because of the low volume of the solution, the cations on the precursor are left not only inside the pores (exchanged cations) but also on the external surface, and the entirety of the precursor is expected to remain in the support after drying [30], so that K/Al = 1, 2 or 10.

This technique was carried out with a $V_{solution}/m_{zeolite}$ ratio of 1 mL/g, with the mass of precursor being calculated based on the required K/Al ratio. Each solution prepared was added to a zeolite sample in a glass beaker and left stirring at 500 rpm for 15 minutes, followed by drying in an oven at 60 °C, for an average of 3 hours.

The modifications were carried out with:

- KNO_3, K/Al = 1
- KOH, K/Al = 2, 10.

ION EXCHANGE

In ion exchange (IE), a much bigger volume of solution is needed than in WI [30]. In this procedure, the excess volume solution is added to the zeolite support, under stirring conditions, over a longer period of time so that the cations in the solution gradually replace the cations in the zeolite's pores [30]. The resulting mixture then undergoes physical separation and washing to remove the excess solution, followed by drying [30]. Because the excess solution is removed from the zeolite before drying, so that only exchanged cations remain (inside the pores), the maximum expected K/Al ratio is 1 [30].

This procedure was carried out with a $V_{solution}/m_{zeolite}$ ratio of 20 mL/g, with the mass of precursor being calculated based on the required K/Al ratio. Each solution prepared was added to a zeolite sample in a glass beaker and left stirring at 500 rpm for 24 hours to ensure a complete cation exchange. The samples were then centrifuged at 5000 rpm for 9 min, decanted, washed with deionized water and centrifuged again at 6000 rpm for 5 min, after which they were left to dry overnight in an oven at 60 °C.

The modifications were carried out with:

- KNO_3, K/Al = 1, 10
- KOH, K/Al = 2, 10.

Table 3 summarises the samples prepared.

Table 3 – Original and modified zeolite samples

Zeolite	Si/Al	Modification technique	Exchanged cation origin	K/Al	Sample name
Beta, β (protonic form)	150	–	–	0	βOS
		Wet Impregnation (WI)	KNO_3	1	βWIKNO$_3$1
			KOH	2	βWIKOH2
				10	βWIKOH10
		Ion Exchange (IE)	KNO_3	1	βIEKNO$_3$1
				10	βIEKNO$_3$10
			KOH	2	βIEKOH2
				10	βIEKOH10

CALCINATION

Calcination is a thermal treatment that can improve the catalytic activity of heterogeneous catalysts [2]. During calcination, the remaining impurities in the zeolite are thermally decomposed, resulting in a better ordered zeolite structure [2]. All samples (original and modified zeolite) were calcined in a *Carbolite Furnaces RHF 1600* calcination furnace. The calcination programme used was as follows:

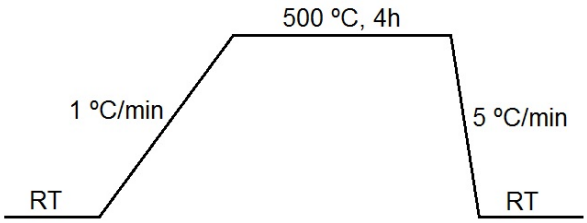

Figure 8 – Calcination programme used on the zeolite samples

3.2. CHARACTERISATION TECHNIQUES

To study the physical and chemical properties of the zeolite samples, a number of techniques were used. A brief description of these techniques is given below.

SCANNING ELECTRON MICROSCOPY

SEM is an analytical technique that evaluates the morphology of a given heterogeneous sample by scanning it with a focused beam of (primary) electrons. This electron beam is swept in a raster pattern through the sample's surface to form images, or statically, to perform a single position analysis [31]. The electrons in the beam interact with the atoms in the sample producing different signals, such as secondary electrons, backscattered electrons or characteristic X-rays [31]. Secondary and backscattered electrons are the most relevant signals emitted because their fluctuation is related to differences in the sample's surface topography [31]. The 3D look of the SEM images is, for the most part, a result of the ample depth of field of the instrument [31].

The X-rays previously mentioned are characteristic of the elements within the sample and can be measured by energy-dispersive X-ray spectroscopy (EDS). In EDS, X-ray photons are converted into voltage signals proportional to them [31]. The resulting spectrum displays the X-ray photon count as a

function of X-ray energy, for the different elements in the sample. EDS systems are usually integrated into SEM instruments.

SEM/EDS sample preparation and loading used in this work were simple: a small amount of powdered sample was pressed at approximately 0.5 ton and placed on an aluminium specimen stub covered with a carbon based, electrically conductive, double sided adhesive disc, known as a Leit tab. The specimen stub was then attached to the sample holder in the SEM instrument, located in the evacuation chamber. The analysis was started after the chamber was closed and evacuated.

The instruments used to analyse the BEA-150 samples were a *Hitachi TM3000* microscope, with a *Bruker Quantax 70 EDS* analytical system attached for elemental analysis, operating at *Analy* or *15 kV* observation modes, respectively.

X-RAY DIFFRACTION

In powder XRD, the structure and crystallinity of a given polycrystalline material can be determined. In a powder diffractometer, an accelerated electron beam hits a metal source (usually copper) generating X-rays. The generated X-rays then hit the polycrystalline sample and are diffracted and reflected towards a detector, known as a Bragg-Brentano detector [32]. The X-ray beam, the sample holder and the detector are all in the same plane throughout the run of the experiment, and the detector moves one-dimensionally in a varying pre-set range of angles [32].

When an X-ray hits a crystal's atoms, its electrons start vibrating with the same frequency as the X-ray, which can cause constructive (in phase) or destructive (out of phase) interferences. In the case of polycrystalline samples, the X-ray hits parallel crystal planes, separated by an interplanar distance, *d*, also known as *d*-spacing, as shown in Figure 9 [32] [33]. For both diffractions to be in phase, the lower beam shown in the image below needs to travel an additional distance, equal to $\overline{AB}+\overline{BC}$, known as the path difference [32] [33].

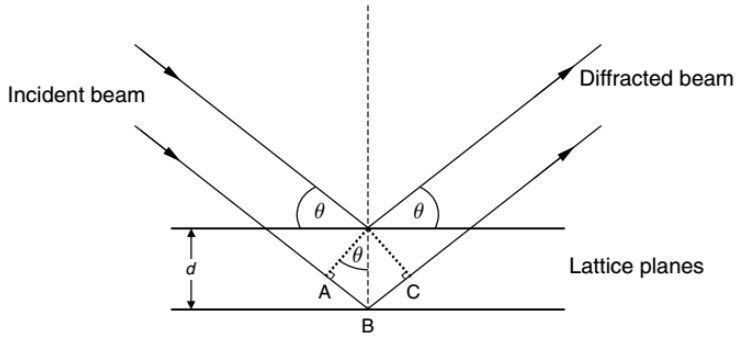

Figure 9 – Diffraction and reflection of radiation through two parallel crystal planes [33]

The path difference can be rewritten in terms of the angle θ, by means of trigonometric relationships:

$$\overline{AB} + \overline{CD} = 2d \cdot \sin\theta \quad (1)$$

If the beams are in phase, i.e. causing constructive interferences, the path difference is equal to an integer multiple, n, of the X-ray wavelength, λ, which translates into Bragg's Law[2] [32] [33]:

$$n\lambda = 2d \cdot \sin\theta \tag{2}$$

When Bragg's equation is satisfied the reflected rays will be detected by the Bragg-Brentano detector, originating different peaks in XRD patterns, where each peak corresponds to a crystallographic plane. XRD patterns display peak intensities as a function of detector angle, 2θ, measured according to the scheme in Figure 10.

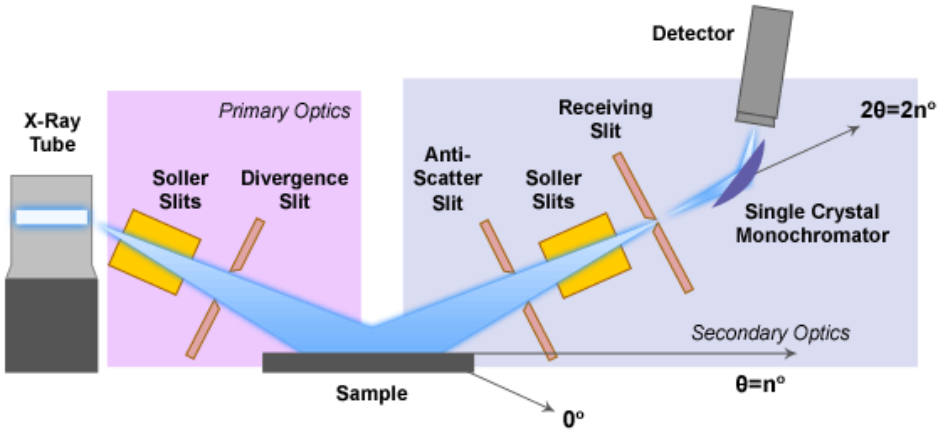

Figure 10 – Bragg-Brentano type diffractometer (adapted from [34])

XRD sample preparation and loading used in this work was relatively simple: the powdered sample was carefully deposited and uniformly smeared across a diffraction plate, after which it was loaded onto the sample holder in the XRD machine; the experimental parameters were set and the programme was started.

The equipment used was a *Bruker D8 Advance* with CuKα radiation (λ = 1.5406 Å), 40 kV voltage and 40 mA amperage. The patterns were collected over a 2θ range between 5 – 60°, with a coupled 2θ/θ scan type, a 0.02° step and a speed of 0.7 s/step.

INFRARED SPECTROSCOPY

Infrared (IR) spectroscopy is one of the most widely used techniques in zeolite science, due to its wide characterisation applications [35]. The most commonly used IR spectrometer is a FTIR spectrometer. FTIR stands for Fourier Transform Infrared, and the basic principle behind it is the conversion of the raw data collected into a spectra via Fourier transform.

The main component of a FTIR spectrometer is a Michaelson interferometer, illustrated in Figure 11. In an interferometer an IR source emits an IR beam that is divided in two by a beamsplitter (usually made of KBr); one of the split beams hits a fixed mirror, while the other hits a moving mirror that moves in the same axis as the incident beam [36] [37]. Both beams are then reflected back towards the beamsplitter, where they are recombined and sent through the sample, which absorbs some of it, and towards the detector [36] [37]. The resulting interferogram is then converted into a spectrum via Fourier

[2] For XRD, n = 1 is the only relevant solution to Bragg's Law [33]

transform. If the position of the moving mirror is such that the reflected beam is in phase with the fixed mirror's reflected beam, the combined beams will result in a constructive interference, which will translate in a peak in the interferogram; if the beams are out of phase, then there will be destructive interference and no peak will appear in the interferogram [36] [37]. The number of times the moving mirror moves back and forth accounts for the number of scans taken, which will then be averaged to obtain the final spectrum [36]. The higher the number of scans, the smaller the noise level in the final spectrum will be, i.e. the better the quality of the spectrum will be [36].

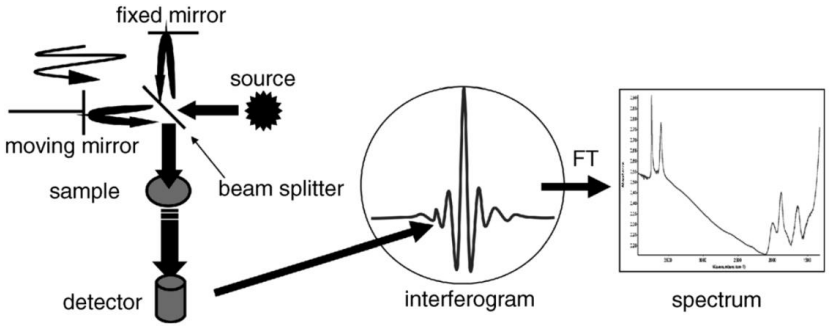

Figure 11 – Layout of an interferometer and conversion of an interferogram to IR spectrum [37]

FTIR spectra usually plot absorbance (A, a.u.) as a function of wavenumber (ν, cm^{-1}), with wavenumber being presented by convention from higher to lower values, from left to right. Absorbance is a measure of the amount of light absorbed by a given sample. It is known that molecular bonds vibrate when they absorb light, hence this absorbed light corresponds to the vibrational frequencies of specific bonds or groups within the sample. For IR light to be absorbed, however, this bond vibration must not be symmetrical, i.e., the electron density in the bond must not be evenly distributed [38]. As such, and in general, only asymmetric bond vibrations of absorbed IR light appear in IR spectra as peaks.

IR spectroscopy is commonly divided into three categories: near-IR ($\nu > 3000$ cm^{-1}), mid-IR ($\nu = 4000 - 400$ cm^{-1}) and far-IR ($\nu < 300$ cm^{-1}) [35]. For zeolite science, mid-IR is the best category because it includes the regions of the IR spectrum associated with surface OH groups, adsorbed molecules and framework vibrations [35]. Figure 12 summarises the main surface OH groups found in zeolites and their corresponding wavenumbers (stretching frequencies) in the IR spectrum [6].

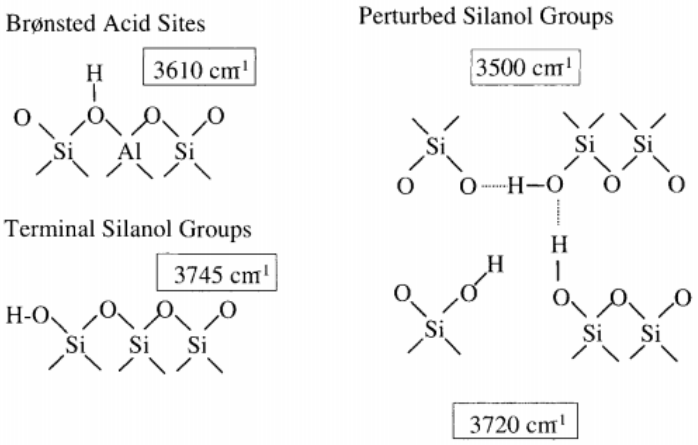

Figure 12 – Types of OH surface groups in zeolites and corresponding stretching frequencies [6]

By the definition of the Beer-Lambert law, absorbance is directly proportional to the concentration of molecules in the sample, and can therefore be used as an indicative of the concentration and strength of active sites in zeolites. By Planck's equation, wavenumber (frequency) is directly proportional to energy, hence, the further to the left (higher ν) the IR band appears in the spectra, the stronger (i.e. the more energetic) that bond will be.

The acidity and basicity of zeolites can be studied in FTIR spectroscopy via the introduction of probe molecules in the system, basic in the first case and acidic in the latter. These probe molecules will adsorb on and interact with the different types of catalytic centres available on the surface of the zeolite. By analysing the adsorption and desorption of probe molecules it is possible to determine the nature, strength, location and amount of these active sites [37]. The choice of probe molecule is subject to the purpose of the analysis in question, although there are some guidelines that should be followed to ensure the proper probe is chosen [37]. In this work, pyridine (Py, *ACROS Organics*, Assay = 99.5%) was used to probe acid sites of the uncalcined samples and acetylene (C_2H_2, *BOC*, $Assay_{min}$ = 98.5%) was used to probe basic sites of the calcined samples. Pyridine is a widely used probe molecule to assess the acidity of zeolites; it interacts with BAS, forming pyridinium ions (PyH^+), adsorbs on LAS (PyL), can form hydrogen bonds with weak acid sites such as silanols (PyOH) and can also be physisorbed [37]. The corresponding bands can all be identified in the IR spectrum in the frequency range of 1700 – 1400 cm^{-1} [37], as can be seen in Figure 13. Acetylene forms hydrogen bonds between its acidic C-H groups and the basic sites in the zeolites' surface and π-complexes with the cations in the zeolite [35] [37]. The corresponding bands can be observed in the IR spectrum in the frequency range of 3300 – 3200 cm^{-1}.

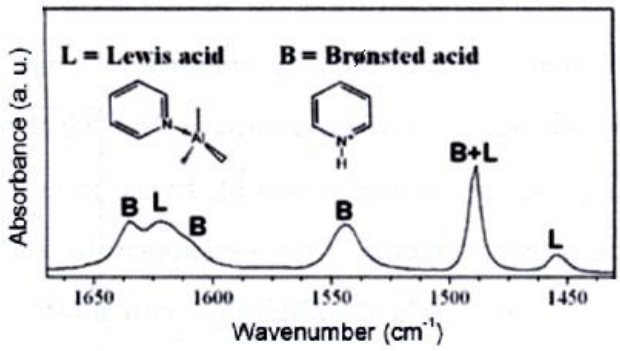

Figure 13 – Typical PyH^+ and PyL IR bands (adapted from [39])

Sample preparation and loading was as follows for both probe molecules used (Py and C_2H_2): the zeolite samples were pressed at approximately 0.5 ton into a self-supporting wafer (ρ = 9 – 12 mg/cm^2); the *in situ* IR cell was opened to atmospheric pressure, disconnected from electric cables, and the upper part containing the sample holder, held by a manual moving chain, was removed from the setup. The wafer was then loaded onto the sample holder, the upper part reattached to the IR cell, the electric cables connected, and the entire system closed to the atmosphere and pressurised.

The activation programme was run overnight according to the scheme in Figure 14. Post activation, the system was purged with N_2, starting approximately one hour before data collection began, and

background spectra were collected. After one hour, the first spectrum (pre-adsorption) was collected at 150 °C for Py and 30 °C for C_2H_2.

For Py adsorption, an excess volume of Py of 1 µL was injected into the cell to ensure full coverage of the active sites. The excess Py was removed by way of pressure gradient after a few minutes. Py-TPD was run according to the scheme in Figure 15. It should be noted that not all samples needed to run the full range of desorption temperatures. After the final desorption temperature, the sample was removed and a mordenite cleaning disc was loaded, to adsorb the remaining Py inside the IR cell. The cleaning programme was run overnight, following the same setup as the activation programme (cf. Figure 14).

For C_2H_2, after the activation programme was complete, the heating was turned off to allow the sample to cool down from 150 °C to 30 °C. C_2H_2 adsorption was done by releasing quantities of C_2H_2 into the system, measured by way of pressure gradient in two increments, the first of which being approximately 0.5 torr and the last of about 5 torr. In earlier test runs, C_2H_2 adsorption pressures higher than approximately 10 torr were found to be contaminating the samples with acetone, a common solvent found in acetylene gas containers for safety reasons, by the appearance of the corresponding peak in the IR spectra. To help prevent sample contamination by acetone, the mixture was kept chilled in its glass container by liquid N_2 in an external Dewar. C_2H_2 was first left to naturally desorb by pressure gradient between the cell and the vacuum system, for circa 30 mins. Afterwards, when needed, C_2H_2-TPD was run according to the scheme in Figure 16. After the last desorption temperature was run and given that the system didn't need an additional cleaning programme as was the case with Py, the sample was removed and a new sample was loaded to run the activation programme overnight (cf. Figure 14).

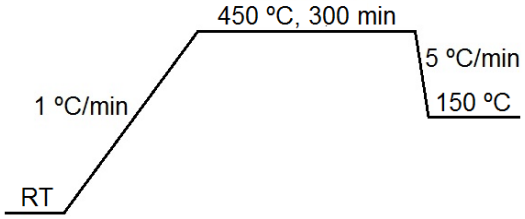

Figure 14 – Activation programme used in the IR experiments

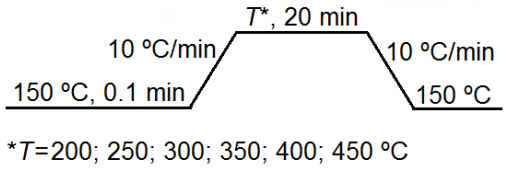

*T=200; 250; 300; 350; 400; 450 ºC

Figure 15 – Py-TPD setup used in the IR experiments

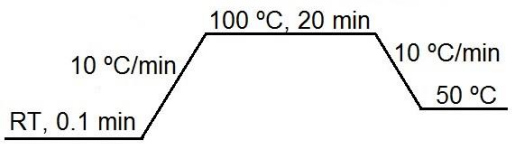

Figure 16 – C_2H_2-TPD setup used in the IR experiments

The experimental setup can be seen in Figure 17. The FTIR instrument used was a *Thermo Scientific Nicolet iS10* spectrometer, with a DTGS KBr detector, a KBr beamsplitter and an optical velocity of 0.4747 cm/s. All spectra were collected in transmission mode, with a resolution of 4 cm^{-1} and 64 scans/spectrum. Background spectra were collected before each main spectra collection. Temperature programmes were set in a *Eurotherm 2416* PID Controller and the vacuum system used was a *Leybold PT50* turbomolecular pump system, with a *Leybold TRIVAC* oil sealed rotary vane pump, a *Leybold TURBOVAC 50* turbomolecular pump and a *Leybol Turbotronik NT 10* electronic frequency converter.

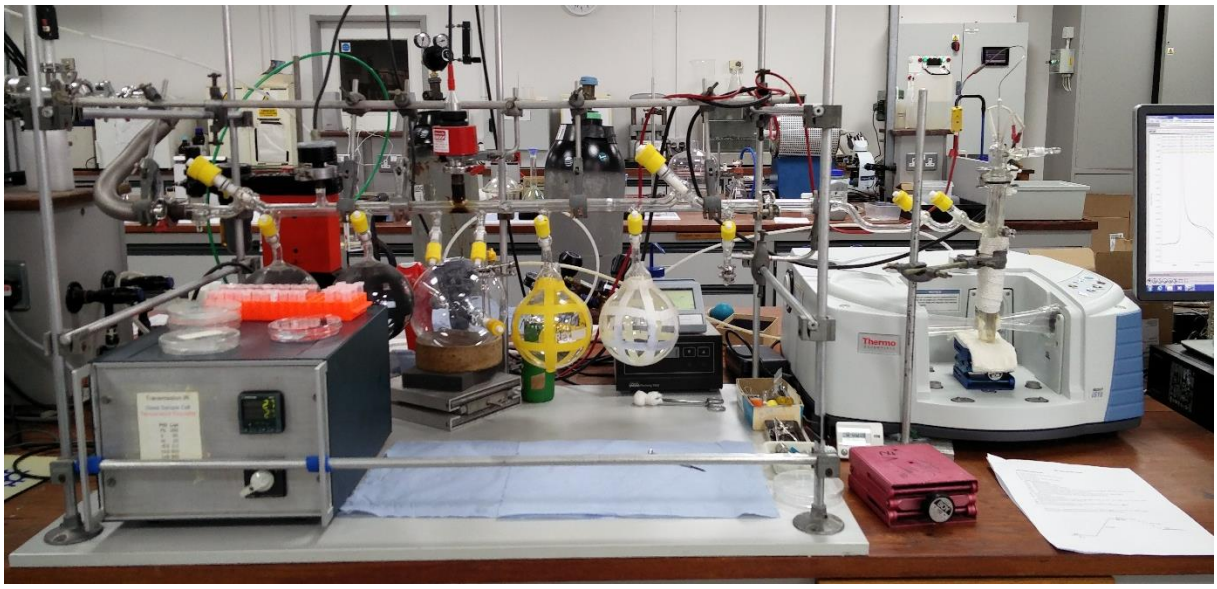

Figure 17 – IR experimental setup

SORPTION EXPERIMENTS

Gas sorption experiments are commonly performed to evaluate the textural properties of porous solids, such as surface area and pore size, volume and distribution. Sorption experiments are most often run with simple gases, such as argon (Ar), krypton (Kr) and nitrogen (N_2) at 77 K, in a liquid nitrogen cryostat, although the latter is recommended by IUPAC [40] [41]. The gas, known as the adsorptive, is released in increasing pressure increments into the sample holder, where it comes into contact with the porous solid, known as the adsorbent, in a phenomenon called physical adsorption (or physisorption). As the gas pressure (i.e. gas quantity) increases, the surface starts to become gradually covered with adsorbed gas molecules (adsorbate) until eventually a monolayer is formed. Now that the entire porous surface is covered with a monolayer of adsorbate, increasing gas pressures will result in the formation of multilayers until the pores are completely filled. IUPAC has classified pores according to their size in the following categories [41] [42]:

- Micropores, with a width of approximately 2 nm or less;
- Mesopores, with a width range of approximately 2 – 50 nm;
- Macropores, with a width greater than approximately 50 nm.

The amount of adsorbed gas is a function of equilibrium pressure, *p*, which is the pressure of adsorptive gas in equilibrium with the adsorbate. The plot of adsorbed amount of gas as a function of

relative pressure, p/p_0, where p_0 is the saturation vapour pressure for a given temperature, is called an adsorption isotherm. According to IUPAC there are six types of adsorption isotherms, labelled from I to VI [40] [41]. IUPAC has also defined four types of hysteresis loops, labelled from H1 to H4, which are associated with capillary condensation in mesopores [40] [41]. The six types of adsorption isotherms and four types of hysteresis loops can be found in Figure 18.

In the plots in Figure 18, the first steep step corresponds to monolayer formation, until the first plateau is reached, in which the monolayer is completely formed (point B in plots II and IV in Figure 18). This plateau corresponds to multilayer formation and its slope varies with the types of pores present in the sample: microporous samples, represented by isotherm I (also known as Langmuir isotherm) will have an almost null slope (seen by the flat plateau in plot I in Figure 18), which means that all the (micro)pores have been filled and increasing adsorptive pressure will have no effect in the adsorbed amount. If there are mesopores this plateau will be steeper until the next step is reached, an even steeper inclination, which corresponds to capillary condensation of the adsorbate. The final plateau step corresponds to complete multilayer filling, i.e. fully occupied pores. Desorption curves usually follow the same, although reverse, path as adsorption curves, the exception being hysteresis loops, where the desorption branch is parallel either vertically (plots IV and H1 in Figure 18), horizontally (Plot H4 in Figure 18), or an intermediate of the two (Plots V, H2 and H3 in Figure 18), to the adsorption branch. Type II isotherms are usually associated with macroporous or non-porous solids, type III with non-porous and non-wetting solids, type IV with mesoporous solids, type V with non-wetting mesoporous solids and type VI with extremely well ordered non-porous solids [40] [41]. H1 hysteresis loop is associated with aggregated porous materials with a small pore size distribution, H2 with mesoporous materials with interconnected bottle-shaped pores, H3 with non-rigid pore structures between particle grains and H4 with non-rigid pore structures between flat plates [40].

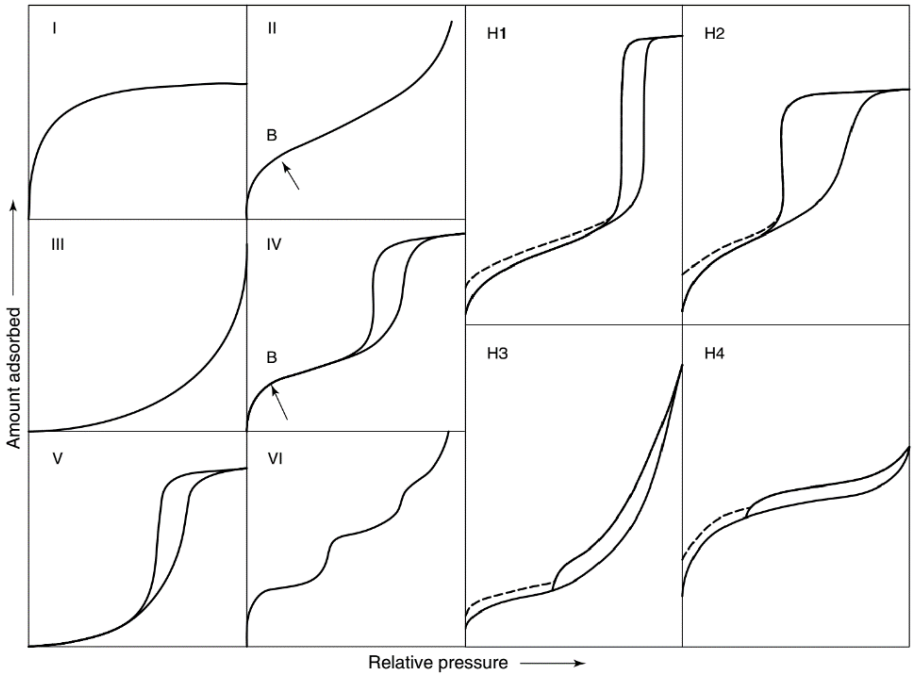

Figure 18 – Adsorption isotherms (I–VI) and hysteresis loops (H1–H4) defined by IUPAC (adapted from [41])

Sample preparation and loading was as follows: a weighed amount of sample (m = 22 – 27 mg) was placed in a sample holder, a 9 mm large bulb cell (with an inner diameter of 7 mm), and loaded into the outgasser station, to be outgassed under heating conditions to remove surface contaminants and moisture. Outgassing and activation were run overnight, with the activation programme run according to the scheme in Figure 19. Following activation the sample was left in the outgasser station to cool down naturally until about 50 °C, after which it was degassed. After degassing and naturally cooling down, the sample holder was transferred to the sorption station and the programme was started. After about 30 – 40 min a Dewar container filled with liquid nitrogen started to rise towards the sample holder, plunging it into the cryostat bath. After an additional 20 min the first adsorption data points appeared on screen. The instrument used was a *Quantachrome Autosorb C1*, with nitrogen used as adsorptive gas. Data analysis was performed in the *Quantachrome ASiQwin 3.0* software, and MultiPoint BET (Brunauer–Emmett–Teller) was used to calculate surface area, *t*-plot method was used to estimate micropore volume and external surface area, and DFT (density functional theory) was used to determine pore size distribution and diameter [40] [41] [42].

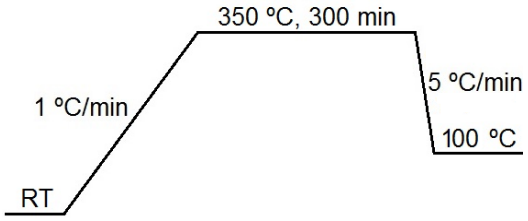

Figure 19 – Activation programme used in the sorption experiments

4. RESULTS AND DISCUSSION

4.1. ZEOLITE MODIFICATION

The amount of potassium needed in each sample was calculated according to the following steps, for a set weight of BEA-150 of 2 g:

- The number of TO_2 (T = Si, Al) moles in 2 g of BEA-150 is given by:

$$MW_{\mathrm{TO_2}} \cong 60\ \mathrm{g/mol} \longrightarrow n_{\mathrm{TO_2}} = \frac{2}{60} = 3.33 \times 10^{-2}\ \mathrm{mol} \tag{3}$$

- The number of Al moles in 2 g of BEA-150 is given by:

$$\frac{n_{\mathrm{Al}}}{n_{\mathrm{TO_2}}} = \frac{1\ \mathrm{Al}}{(150+1)\ \mathrm{TO_2}} \longrightarrow n_{\mathrm{Al}} = \frac{1}{151} \cdot 3.33 \times 10^{-2} = 2.2 \times 10^{-4}\ \mathrm{mol} \tag{4}$$

- The amount of KNO_3 needed as a source of K, for 2 g of BEA-150 is given by:

$$MW_{\mathrm{KNO_3}} = 101.11\ \mathrm{g/mol};\quad \mathrm{Assay} = 99\%$$

$$n_{\mathrm{KNO_3}} = n_{\mathrm{K}} = x \longrightarrow m_{\mathrm{KNO_3}} = \frac{101.11 \cdot x}{0.99}, x = (1, 10) n_{\mathrm{Al}} \tag{5}$$

- The amount of KOH needed as a source of K, for 2 g of BEA-150 is given by:

$$MW_{\mathrm{KOH}} = 56.11\ \mathrm{g/mol};\quad \mathrm{Assay} = 86.15\%$$

$$n_{\mathrm{KOH}} = n_{\mathrm{K}} = y \longrightarrow m_{\mathrm{KOH}} = \frac{56.11 \cdot y}{0.8615}, y = (1, 2, 10) n_{\mathrm{Al}} \tag{6}$$

The theoretical and experimental values are listed below in Table 4. All components were weighed in an *Ohaus Adventurer AR0640* analytical balance, with a maximum capacity of 65 g and a readability of 0.0001 g.

Table 4 – Theoretical and experimental quantities for the modified samples

Sample Name	Theoretical		Experimental	
	$m_{\text{BEA-150}}$ (g)	$m_{\text{K source}}$ (g)	$m_{\text{BEA-150}}$ (g)	$m_{\text{K source}}$ (g)
βWIKNO3_1	2	0.0225	2.0032	0.0230
βWIKOH2		0.0288	2.0023	0.0299
βWIKOH10		0.1438	2.0029	0.1440
βIEKNO3_1		0.0225	2.0033	0.0229
βIEKNO3_10		0.2255	2.0055	0.2279
βIEKOH2		0.0288	2.0028	0.0298
βIEKOH10		0.1438	2.0030	0.1444

4.2. SEM/EDS

SEM images were collected in ordered to study the shape and size of the particles, whereas EDS measurements were taken to determine the elemental composition of the zeolite samples.

The following sets of images illustrate the SEM images collected, in varying magnifications.

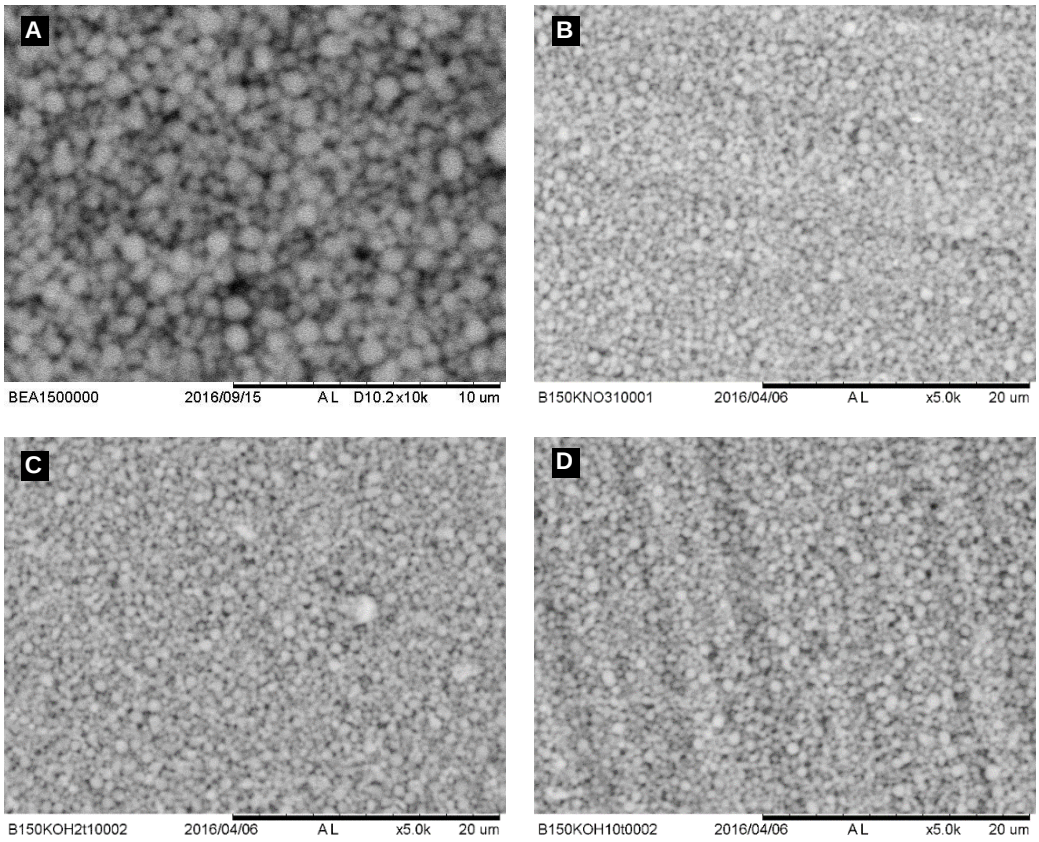

Figure 20 – SEM images of samples βOS (A), βWIKNO$_3$1 (B), βWIKOH2 (C) and βWIKOH10 (D)

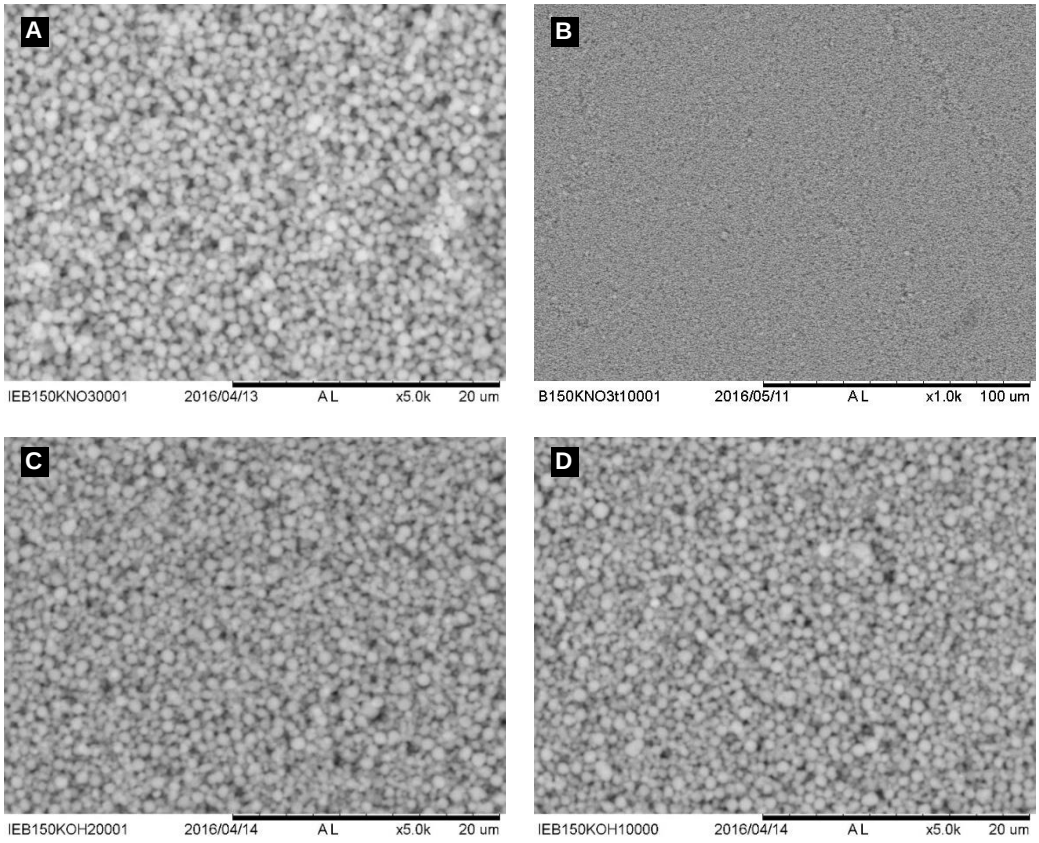

Figure 21 – SEM images of samples βIEKNO$_3$1 (A), βIEKNO$_3$10 (B), βIEKOH2 (C) and βIEKOH10 (D)

As can be seen from the images in Figures 20 and 21, the particles are evenly distributed in the samples and are approximately homogenous in shape and size. From Figure 20A it can be concluded that the average particle size sits around 1 μm[3]. As previously mentioned, the crystallite size for zeolite beta is usually in the rage of 20 – 50 nm [23] [24], which can suggest that the particles observed in Figures 20 and 21 are agglomerates of smaller crystallites. It can also be observed that chemical treatment does not appear to affect the particle size and shape, however, as picture clarity severely decreases with magnification, this may not be accurate. Indeed, it is worth noting that from a magnification of 10000 onwards the picture quality made it impossible to distinguish specific details of the particles' morphology.

Following SEM image collection, the samples were subject to EDS measurements, which provided elemental composition, with which it was possible to estimate Si/Al and K/Al ratios. Figure 22 exemplifies an EDS spectrum obtained from sample βWIKOH10. Table 5 presents the Si/Al and K/Al ratios theoretically expected and experimentally obtained from EDS elemental analysis. It is worth noting that every experimental ratio shown in Table 5 represents the mean average of three distinct measurements taken in different areas of the corresponding sample, in order to achieve a higher degree of accuracy in the results.

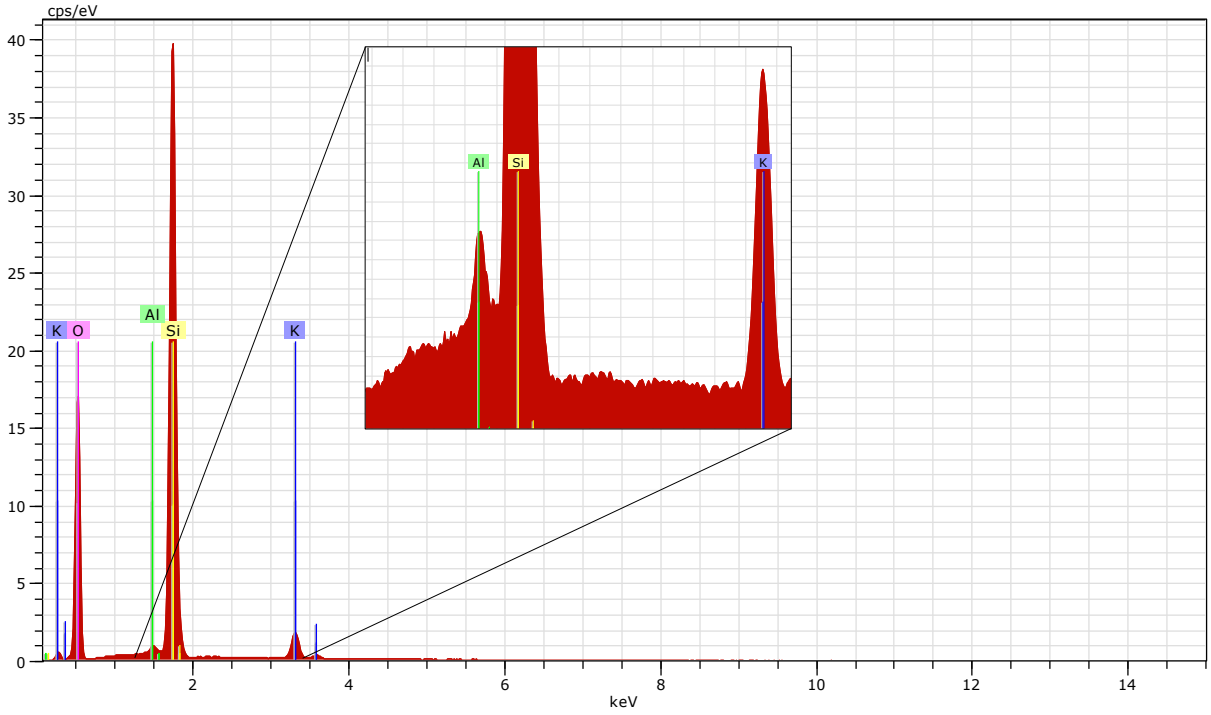

Figure 22 – EDS spectrum of sample βWIKOH10, with an additional zoom in the Al, Si and K region

As can be seen in the spectrum above, the potassium peak extends much higher (i.e. is more intense) than the aluminium peak, as was to be expected, given that there is a 10-fold molar excess of potassium in comparison to aluminium in this particular sample.

[3] The scale for the SEM images is given by the black bar underneath the pictures, which is divided in 10 segments. The value on the bottom left corner of each image corresponds to the total length of the black bar, so that, for example, in Figure 20A, the scale is 10 μm, with each segment measuring 1 μm.

Table 5 – Theoretical and experimental Si/Al and K/Al ratios of the original and modified BEA-150 samples

Sample Name	Theoretical		Experimental	
	Si/Al	K/Al	Si/Al	K/Al
βOS	150	–	76.9	–
βWIKNO$_3$1		1	75.8	0.6
βWIKOH2		2	77.9	1.1
βWIKOH10		10	79.2	5.4
βIEKNO$_3$1		≤ 1	84.1	0.4
βIEKNO$_3$10		≤ 1	72.8	0.7
βIEKOH2		≤ 1	69.6	0.9
βIEKOH10		≤ 1	75.6	4.8

As can be seen above, despite being consistent with each other, the experimental results for the Si/Al and wet impregnation K/Al ratios of all samples are approximately half of what they should be. These results can have different explanations: the detector may be measuring double the amount of aluminium present, either by the electron beam fully penetrating the Leit tab and hitting the aluminium specimen stub underneath or by hitting the stub's borders that are not covered by the Leit tab. This hypothesis has been disproved by testing two other zeolite samples, which were prepared and loaded following the same procedure as the BEA-150 samples. In these new samples, ZSM-5 (Si/Al = 40) and BEA-19 (Si/Al = 19), the Si/Al ratios determined by EDS elemental analysis were, respectively, 35.5 and 18.8, that fall within an acceptable margin of error, and rule out the possibility of the extra aluminium amount detected coming from the specimen stub.

Another possibility lies with the BEA-150 sample used. The Si/Al ratio provided by the manufacturer may only express the framework Si/Al ratio and there can be EFAL species that also contribute to the EDS elemental analysis, increasing the Si/Al ratios of the samples. Furthermore, EDS elemental analysis does not differentiate between framework and extra-framework aluminium. Two additional characterisation techniques can be employed to further study this phenomenon: ^{29}Si MAS NMR and solid-state ^{27}Al NMR. While the former can be used to determine the framework Si/Al ratio, the latter can be used to ascertain the presence of EFAL species in the sample. In short, in the ^{29}Si MAS NMR spectra of zeolites, five well-defined intervals of chemical shifts can be distinguished, which represent the five possible environments surrounding a Si atom and are denoted as Si(nAl), $0 \leq n \leq 4$, as can be seen in Figure A1 in Appendix A [43]. The framework Si/Al ratio can be calculated using the signal intensities in the spectra, according to Equation A1 in Appendix A. In ^{27}Al NMR spectra of zeolites, two major chemical shifts can be identified: the first, located in the range of 55 – 70 ppm corresponds to tetrahedrally coordinated framework aluminium (Al^{IV}) and the second, located around 0 ppm corresponds to octahedrally coordinated EFAL (Al^{VI}) [43]. ^{27}Al NMR and ^{29}Si MAS NMR were run on the original sample (βOS) by a senior academic staff member, and the resulting spectra can be found in Appendix A. In the ^{29}Si MAS NMR two peaks can be identified, which correspond to Si(1Al) and Si(0Al), as was expected due to the low Al content in the sample (Si/Al = 150). However, the calculated framework Si/Al ratio by Equation A1 was 19.1, significantly lower than the expected 150. This can be explained by the existence

of SiOH groups, of which one of the two possible signals, denoted by Si(3Si,1OH), coincides with the Si(1Al) signal, increasing its intensity in the spectrum [6] [43]. As a result, framework Si/Al ratio calculated via ^{29}Si MAS NMR spectrum is not accurate and no further conclusion can be taken from it to explain the origin of the 100% excess of aluminium given by the EDS elemental analysis. Through ^{27}Al NMR, EFAL was found to be present in βOS, although with a relative peak intensity of approximately one-third of the relative intensity of the Al^{IV} peak, and a much narrower peak width than that of Al^{IV}. These results show that EFAL is not in a sufficiently high quantity to be responsible for the 100% excess of aluminium determined by the EDS elemental analysis.

One other, simpler, explanation can be given to this phenomenon: The SEM/EDS apparatus used is incapable of accurately detecting an amount of aluminium as low as the one found in BEA-150. This seems to be the case as the Si/Al ratio determined in the samples with a much higher aluminium content, ZSM-5 and BEA-19, were accurate within an acceptable margin of error.

The ion exchange K/Al ratios are all within the maximum expected value, with the exception of the last sample, βIEKOH10, that is circa five times higher than expected. This can be explained by the large molar excess of KOH, a strong base, added to this sample. The KOH, in addition to reacting with the bridging OH groups in the zeolite, thus exchanging H^+ with K^+, can also be reacting with SiOH groups, increasing the amount of K^+ cations in this sample, therefore resulting in a K/Al ratio greater than the theoretical limit of 1. This hypothesis can be evaluated by the analysis of FTIR spectra, found in the coming pages, in Subchapter 4.4. It is worth noting that even though sample βIEK$NO_3$10 was also prepared with a molar excess of 10 in regards to Al, KNO_3 is an ionic salt that is practically neutral in aqueous solution, and therefore would not react with SiOH groups.

4.3. XRD

XRD patterns were taken to study the crystallinity of the BEA-150 samples. In addition to the first eight samples, the crystallinity of the corresponding calcined samples was also measured by XRD. This provided a better understanding of the effect calcination has on the different samples.

The XRD patterns of the eight uncalcined original and modified BEA-150 samples can be found in Figure 23. The well-defined characteristic peaks of zeolite beta can be seen in Figure 23 [44]. Furthermore, it can also be concluded that the BEA-150 zeolite samples used are composed of approximately 50 – 60% polymorph B (cf. Figure B1, Appendix B) [44]. Minor noise and background interferences were detected in all patterns, which suggests that the material is amorphous to some extent. The broad peaks observed are an indication of this structure's disordered nature, particularly peak number 1 in Figure 23, which corresponds to the reflection of the crystallographic plane (001) (cf. c direction in Figure 7). The patterns for the samples that have been treated with KOH show a clear loss of crystal structure that can be attributed to desilication caused by this strong base, which results in the destruction of the structure [45]. The five peaks numbered in Figure 23 have been attributed to the crystallographic planes listed in Table 6 [21].

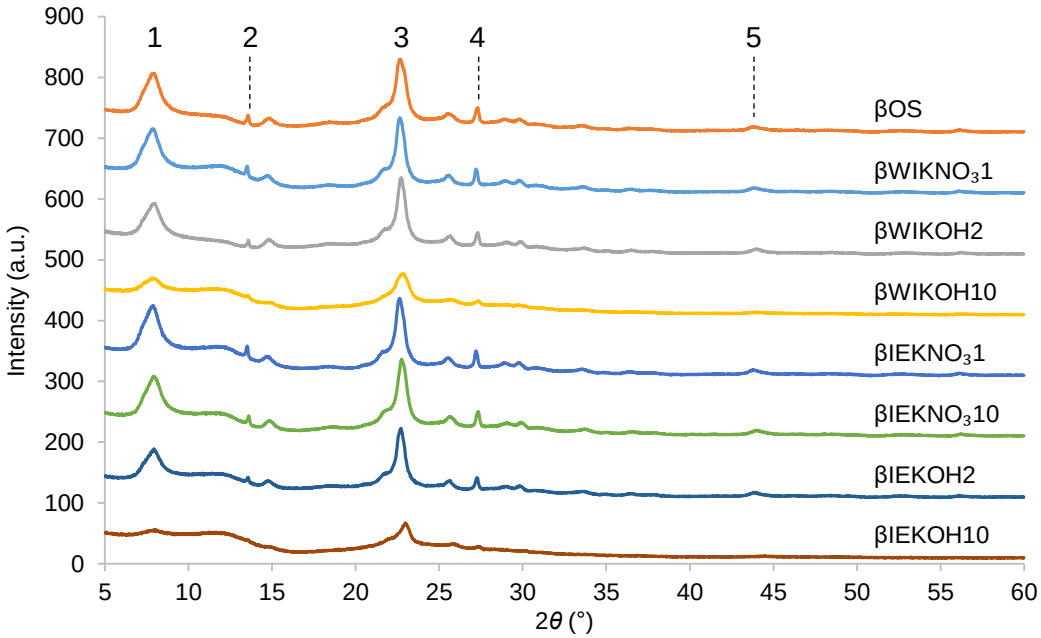

Figure 23 – XRD patterns of the uncalcined original and modified BEA-150 samples

Table 6 – Crystallographic planes identified on BEA-150 samples [21]

Peak	2θ (°)	Crystallographic plane
1	7.8 – 8.0	(001)
2	13.5 – 13.6	(004)
3	22.4 – 23.0	(302)
4	27.1 – 27.4	(008)
5	43.6 – 44.5	(600)

To better compare the effects of each modification treatment, a relative crystallinity was calculated according to Equation 7, using the original sample, βOS, as reference. The results are presented below, in Table 7.

$$\text{Relative Crystallinity (\%)} = \frac{\sum_{i=1}^{5}(\text{Intensity}_i)_x}{\sum_{i=1}^{5}(\text{Intensity}_i)_{\beta\text{OS}}} \times 100 \quad (7)$$

where i corresponds to each numbered peak in Figure 23 and x corresponds to each modified sample.

Table 7 – Relative crystallinity of the modified BEA-150 samples in regards to βOS

Sample	Relative Crystallinity (to βOS)
βWIKNO3 1	108%
βWIKOH2	94%
βWIKOH10	68%
βIEKNO3 1	113%
βIEKNO3 10	104%
βIEKOH2	91%
βIEKOH10	48%

As can be seen in Table 7, the samples modified with KNO_3 demonstrate a slight increase in relative crystallinity, when compared to the original sample βOS (with H^+ as extra-framework cation). This can be explained by the fact that potassium is a much heavier atom than hydrogen and heavier atoms are stronger X-ray scatterers [32]. As such, the contributions of potassium to the diffraction intensities are in general higher than those of hydrogen. The exception to this, in the scope of this work, is the contributions of potassium to the XRD patterns when its source is KOH, seeing that, as mentioned before, KOH promotes desilication, and therefore loss of crystallinity by structure collapse. Indeed, the results determined by Equation 7 for the samples treated with KOH show a loss of crystallinity in comparison with the original sample, βOS, which was already noticeable in Figure 23.

The following sets of images presented in Figures 24 and 25 show a comparison of each sample pre and post-calcination. Overall, it can be seen that calcination improves the crystallinity of the samples, the exception being the samples treated with KOH with a K/Al molar ratio of 10 (Figures 24D and 25D). The increased crystallinity of calcined samples is related to improvements in contrast between the framework (high electron density) and the pores (zero electron density) [32] [33]. The uncalcined samples can have extra-framework species in their pores, such as water, organic molecules or nitrogen compounds, that contribute to the electron scattering of the sample. However, unlike exchanged cations, these molecules are located more towards the centre of the pores, occupying zero electron density zones, and thus their scattering decreases the overall contrast [32]. Calcination tends to remove these extra-framework molecules, voiding zero electron density zones, which results in better contrasts in the XRD patterns. In the case of the samples treated with KOH with a K/Al molar ratio of 10 (Figures 24D and 25D), as the structure is already severely damaged due to desilication, leaving Al atoms more exposed in the remaining structure, the calcination will cause dealumination [46], further disintegrating these samples' crystalline structures.

To better compare the effect of calcination on the eight samples, Equation 7 was used to determine the relative crystallinity of each calcined sample in regards to its uncalcined form. The results are shown below in Table 8.

Table 8 – Relative crystallinity of the original and modified BEA-150 calcined samples in regards to their uncalcined forms.

Sample	Relative Crystallinity (to uncalcined form)
βOS, calc.	132%
βWIKNO$_3$1, calc.	121%
βWIKOH2, calc.	120%
βWIKOH10, calc.	49%
βIEKNO$_3$1, calc.	115%
βIEKNO$_3$10, calc.	125%
βIEKOH2, calc.	106%
βIEKOH10, calc.	57%

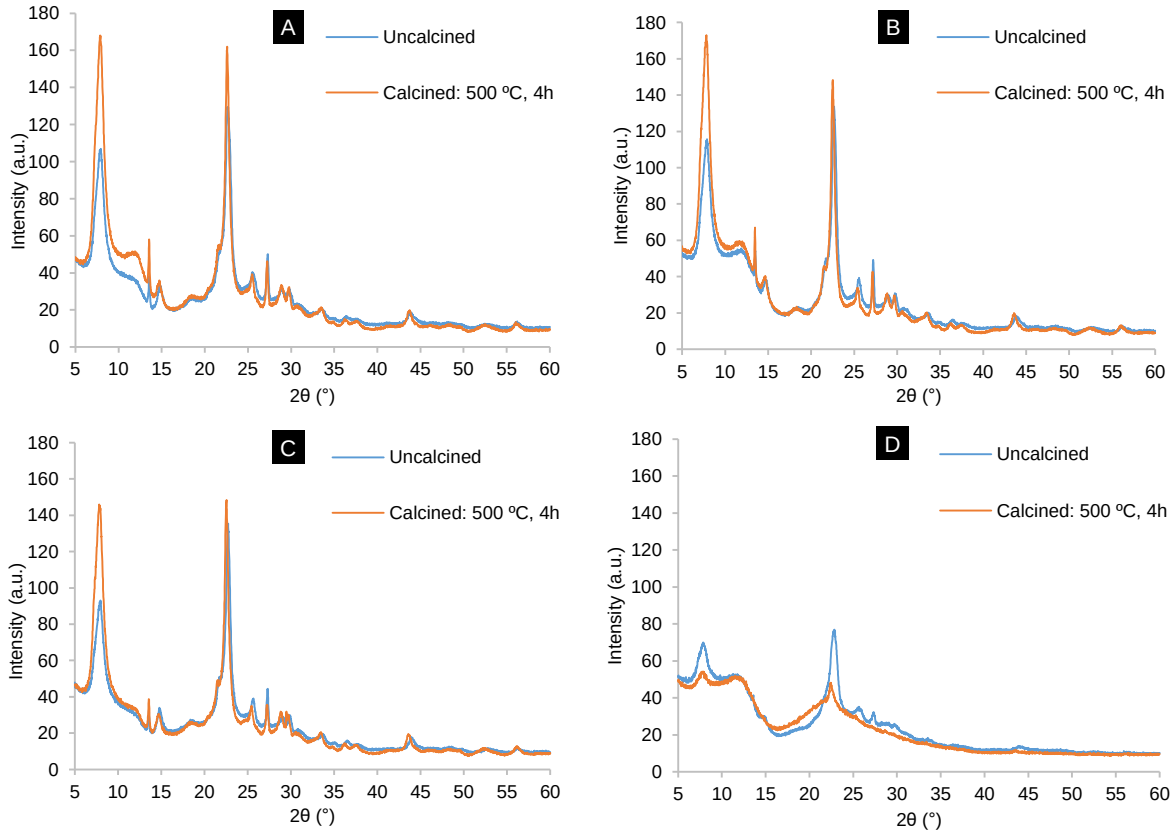

Figure 24 – XRD patterns of samples βOS (A), βWIKNO$_3$1 (B), βWIKOH2 (C) and βWIKOH10 (D), pre and post-calcination

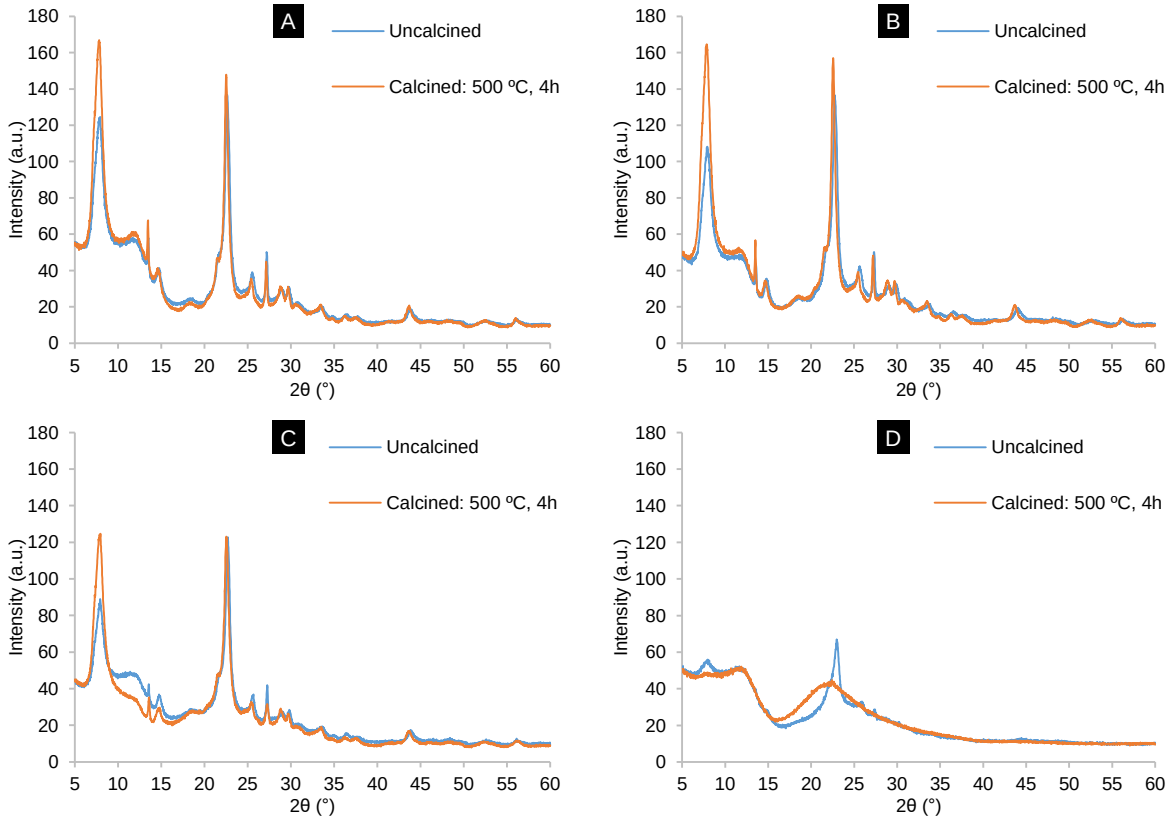

Figure 25 – XRD patterns of samples βIEKNO$_3$1 (A), βIEKNO$_3$10 (B), βIEKOH2 (C) and βIEKOH10 (D), pre and post-calcination

4.4. INFRARED

The IR data collected is presented below. All spectra were analysed in the 4000 – 1400 cm^{-1} region. For the sake of consistency, all spectra were scaled to 10 mg/cm^2. Difference spectra were calculated by subtraction of the first samples' spectra (pre-adsorption), using a subtraction factor of 1.

ACIDITY

The IR spectra of the eight uncalcined original and modified samples, collected post-activation at 150 °C, can be found below in Figure 26. These spectra were collected under vacuum after activation at 450 °C for 300 min (cf. Figure 14).

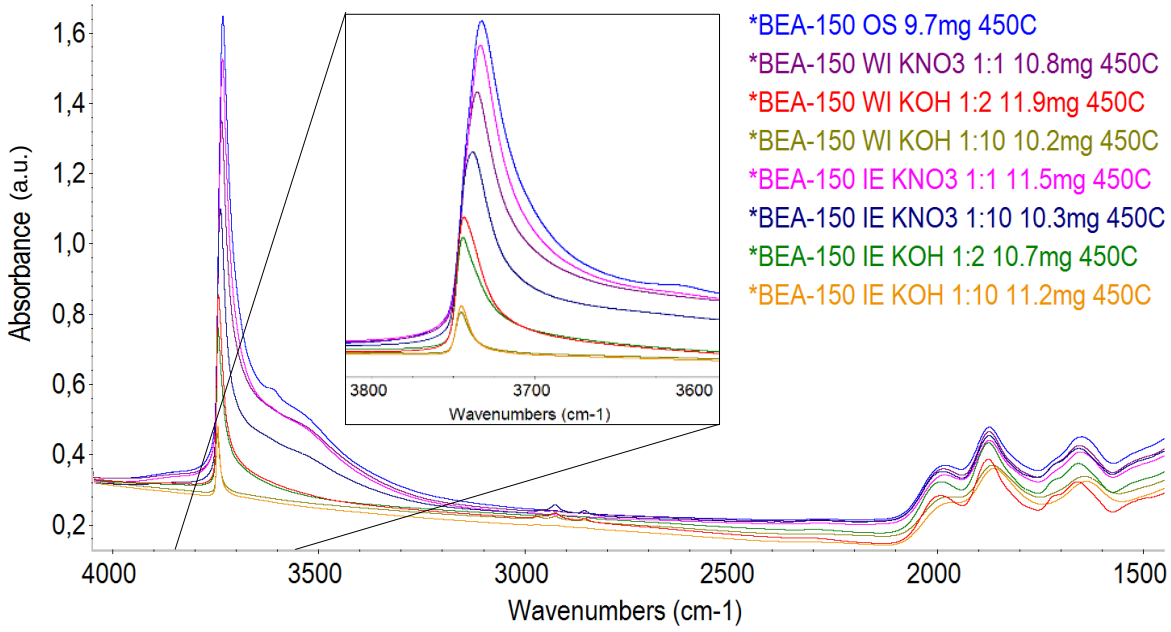

Figure 26 – IR spectra, collected at 150 °C, of the uncalcined original and modified activated BEA-150 samples, with an additional zoom in the SiOH region

Two major bands can be identified in Figure 26: the band characteristic of SiOH groups, located in the range of 3745 – 3732 cm^{-1}, and the band associated with bridging OH groups (BAS), seen only for βOS at 3611 cm^{-1}. The shoulder at around 3500 cm^{-1} can be associated with the existence of perturbed SiOH groups, particularly hydrogen-bonded SiOH nests (cf. Figure 12), or with contaminants such as water or nitrogen compounds (OH and NH stretching frequencies, respectively). The small peaks seen at approximately 3000 – 2800 cm^{-1} correspond to CH stretching vibrations, which should be related to organic contaminants in the samples. The large peaks around 2000 – 1600 cm^{-1} are associated with silicon and oxygen overtones.

Examining Figure 26, it can be clearly seen that the intensity of the SiOH band decreases drastically with increase of potassium content, and that this decrease is further heightened when KOH is the source. These results confirm that KOH (and to a lesser degree KNO_3) is reacting with SiOH groups, originating SiOK groups, as had been theorised previously in Subchapter 4.2. This is the reason behind the increased K/Al ratio of sample βIEKOH10 (as a reminder, it is circa 5 when it should be ≤ 1); there is more potassium in the sample because, apart from reacting with BAS as was to be expected, it is also reacting with SiOH, thus increasing the overall potassium content in the sample and the subsequent

K/Al ratio. Furthermore, as the number of SiOH groups decreases, the peak intensity is gradually shifting to higher frequencies (blueshift[4]), which is an indicative of stronger bonds, i.e., decreased acidity. The SiOH band for the untreated sample, BEA-150 OS, is located at 3732 cm^{-1} which corresponds to internal SiOH groups due to structural defects [47], characteristic of the disordered structure of zeolite beta.

To study the acidity of the BEA-150 samples, pyridine (Py) was used as probe molecule. The adsorption spectra of this probe molecule can be seen below in Figure 27. To better understand the effect of pyridine adsorption, difference spectra were taken by subtracting each spectrum in Figure 27 by the corresponding activated sample's spectrum in Figure 26. The results can be found in Figure 28.

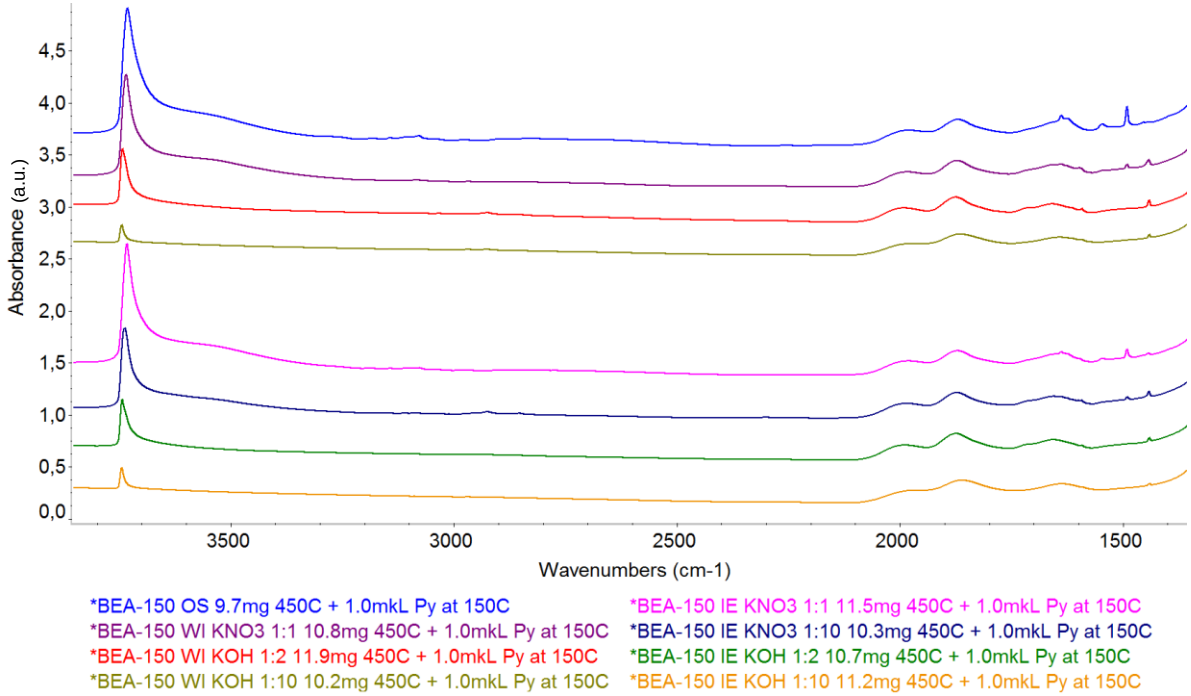

Figure 27 – IR spectra of the BEA-150 samples after pyridine adsorption at 150 °C

In the difference spectra in Figure 28 negative peaks correspond to band positions in the initial spectra (activated samples) and positive peaks correspond to the positions of those bands in the current spectra (post Py adsorption). The trend in SiOH disappearance can be seen in the region of 3745 – 3732 cm^{-1}, as can the disappearance of the bridging OH group at 3611 cm^{-1}. As mentioned before, the latter is a result of the transfer of the acidic proton from BAS (Si-O(H)-Al) to pyridine, originating pyridinium ions (PyH^+) [48].

[4] Blueshift is the designation given to decreases in wavelength, i.e. increases in wavenumber and its name is related to the visible light spectrum, in which the colour blue corresponds do lower wavelengths. It is the opposite of redshift.

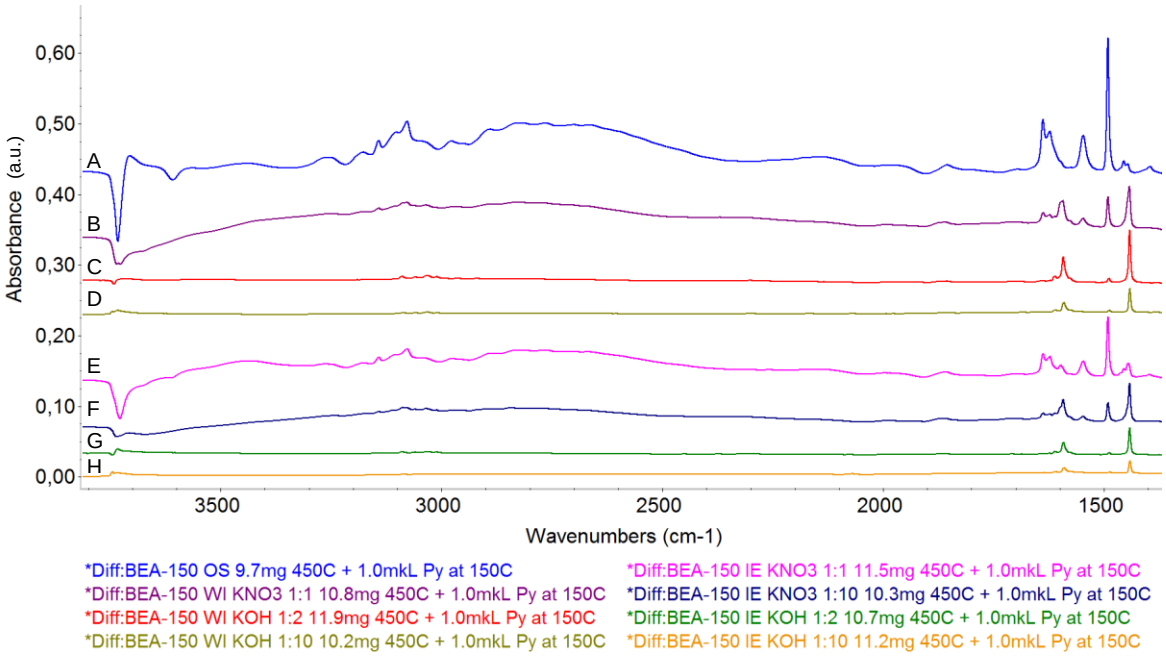

Figure 28 – Difference spectra of pyridine post-adsorption

Difference spectra allow a better analysis of the existing peaks that could otherwise be difficult to accomplish. Indeed, and unlike in the spectra of Figure 26, in Figure 28 it is possible to visualise the existence of a small BAS peak in spectrum E (sample βIEKNO$_3$1, “BEA-150 IE KNO3 1:1”) that has reacted with pyridine, resulting in a negative peak at 3611 cm^{-1}.

The IR bands corresponding to pyridine adsorption on zeolites are commonly found in the frequency range of 1700 – 1400 cm^{-1} (cf. Figure 13). Figure 29 displays a zoom in this IR region of the difference spectra in Figure 28. Twelve peaks have been identified in the spectra in Figure 29 and summarised in Table 9.

Examining Figure 29, it can be seen that the samples treated with KOH (spectra C, D, G and H) present no PyH$^+$ peaks (peaks 1 and 7), which shows that there are no BAS in those samples, and although a small amount of LAS can be found, basicity appears to have been achieved. The spectra of the samples treated with KNO$_3$ (B, E and F) show small PyH$^+$ peaks in comparison with the original sample’s spectrum (A), which was to be expected; furthermore, it can be concluded that given the absence of BAS in spectra B and F (as seen in Figure 28), PyH$^+$ peaks correspond to weaker acidic interactions, such as those between pyridine and SiOH groups. In IE, mobile species like EFAL (the most common type of LAS) tend to be removed in the excess solution, and therefore, PyL in the corresponding spectra may be related to other types of LAS, such as extra-framework cations or aluminium in structural defects.

Peak 4 appears only in spectra B, E and F, and as such it can be suggested that it is associated with a weak hydrogen bond between one C-H group from Py and one oxygen from remaining nitrate groups, resulting in a C-H···O type of bond. This, however, seems unlikely, as remaining nitrate groups would have been decomposed during sample activation. A simpler explanation can be given: peak 4 can be related to a weak type of PyL.

Peak 5 is present in all spectra of the modified samples, with the exception of spectrum E, which is an indicative that this peak is related to an interaction of Py with potassium ions, that exist in inferior quantities in the sample of spectrum E. Furthermore, considering the spectra in Figure 26, it can be suggested that this interaction corresponds to a physisorption of Py in SiOK groups, and, as such, this could be the reason for the absence of peak 5 in spectrum E (Figure 26 shows an almost null decrease in SiOH groups in the spectrum of sample βIEKNO$_3$10, "BEA-150 IE KNO3 1:1").

Peak 6 appears in spectra B, C, E, F and G, which correspond to potassium-containing samples that do not show severe structural damage, and can be attributed to weak PyL or H-bond to remaining (and extremely weak) acid sites.

Peak 7 represents the most notable PyH^+ peak, which corresponds to C-N vibrations, and its appearance only in spectra A, B, E and F, reinforces that only these samples have a certain degree of acidity left.

Peak 8 appears in all spectra in different intensities; in spectra C, D, G and H, that correspond to samples modified with KOH, this peak is slightly shifted to lower frequencies (redshift[5]) which can be an indicative of these samples' basicity in comparison with the other samples. In these spectra peak 8 would correspond to extremely weak PyL or H-bond to weak acid sites.

Peak 9 is associated with iminium (IM) ions generated from proton attack to PyL and appears only in spectra A and E, which suggests that the formation of iminium ions is related to BAS and LAS. Indeed, it has been observed in Py-TPD that peak 9 increases with increasing desorption temperature, whereas, particularly peaks 7 and 10 (the latter being the most notable PyL peak, associated with C-N vibrations and only visible in spectra A and E) decrease with increasing temperature. Py-TPD has shown an almost complete pyridine desorption from BAS and an incomplete desorption from LAS.

The relative intensities (to post Py adsorption at 150 °C) of peaks 7, 9 and 10 for sample βOS (spectrum A, "BEA-150 OS") have been plotted as a function of temperature in Figure 30. The relative intensities of PyH^+ and IM ions show symmetrical parabolic trends, with a slight variation in intensity until a desorption temperature of 300 °C is reached, and a sharp decrease or increase, respectively, thereafter. This symmetrical trend shows that pyridine desorption from BAS is a crucial factor in the formation of IM ions; the steady decrease of PyL associated with peak 10 may indicate that these are not the only type of PyL responsible for the formation iminium ions. The steepness of the desorption curve of pyridine from BAS is an indicative that there are strong acid sites in the original sample, βOS, as per the definition of BAS. The mild and incomplete desorption of pyridine from LAS is suggestive of the very strong nature of these sites, i.e., pyridine still remains adsorbed to LAS at high temperatures.

Peak 11 appears in spectra A and E, and as a shoulder in spectra B and F and is associated with Py physisorbed to hydrogen and can be considered weak PyL.

[5] Redshift is the designation given to increases in wavelength, i.e. decreases in wavenumber and its name is related to the visible light spectrum, in which the colour red corresponds do higher wavelengths. It is the opposite of blueshift.

Lastly, peak 12 corresponds to Py physisorbed to potassium (Py-K) and is visible in spectra B, C, D, F, G and H. Py-TPD has shown an almost immediate desorption of Py from potassium in these six spectra, which is an indicative of weak bonding. The relative intensities of peak 12 for these samples have been plotted as a function of temperature in Figure 31.

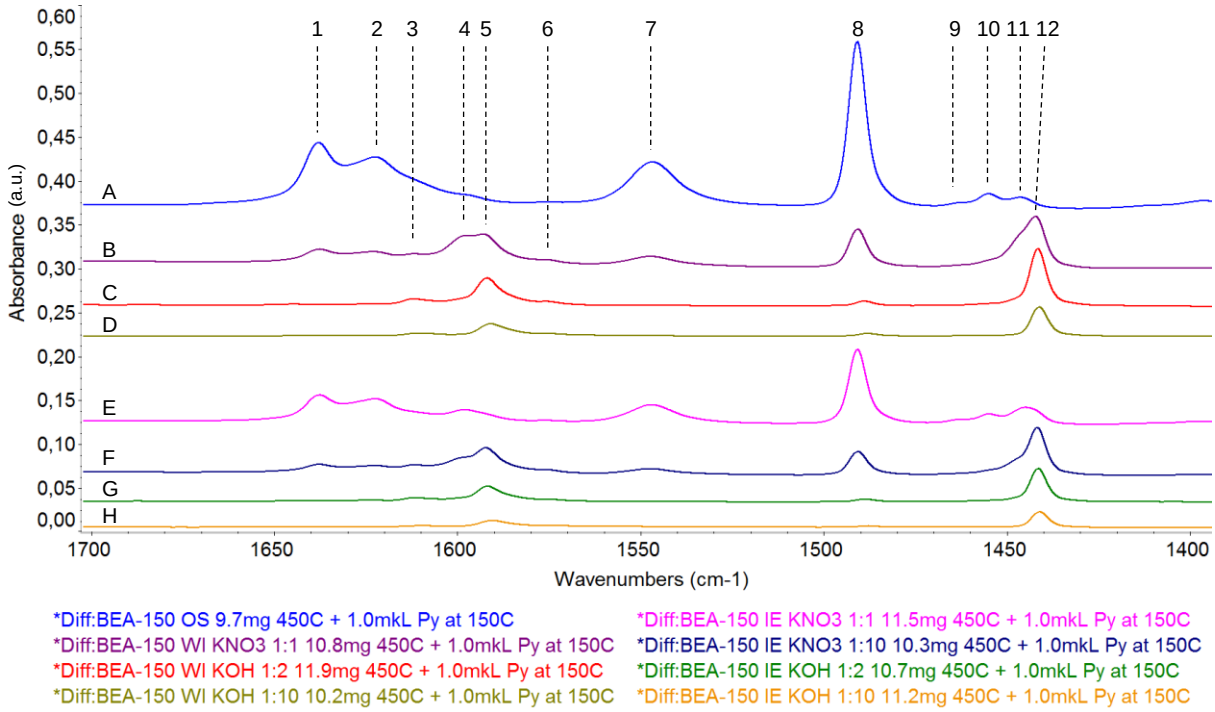

Figure 29 – Difference spectra of pyridine post-adsorption (zoom in the 1700 – 1400 cm^{-1} region)

Table 9 – Pyridine adsorption peaks in the IR region of 1700 – 1400 cm^{-1}

Peak	*v* (cm^{-1})	Spectra	Species
1	1638	A B E F	PyH^+ (8a vibrational mode, ν_{CC}) [37]
2	1622	A B E F	PyL (8a vibrational mode, ν_{CC}) [24] [37]
3	1612	B C D E F G	PyL (8a vibrational mode, ν_{CC}) [37]
4	1599	B E F	Suggestive of weak PyL (8a vibrational mode, ν_{CC}) [37]
5	1592	B C D F G H	Suggestive of Py physisorbed to K (in SiOK groups)
6	1575	B C E F G	PyL (8b vib. mode, ν_{CC}); H-bond to weak acid sites [37]
7	1547	A B E F	PyH^+ (19b vibrational mode, ν_{CN}) [37]
8	1491 – 1489	A B C D E F G H	PyH^+, PyL and H-bond (19a vib. mode, ν_{CN}) [24] [37]
9	1463	A E	Iminium ions [24] [48]
10	1456	A E	PyL (19b vibrational mode, ν_{CN}) [24] [37]
11	1446	A B E F	Py physisorbed to H (can be considered PyL) [24] [49]
12	1443 – 1441	B C D F G H	Py physisorbed to K (can be considered PyL) [49]

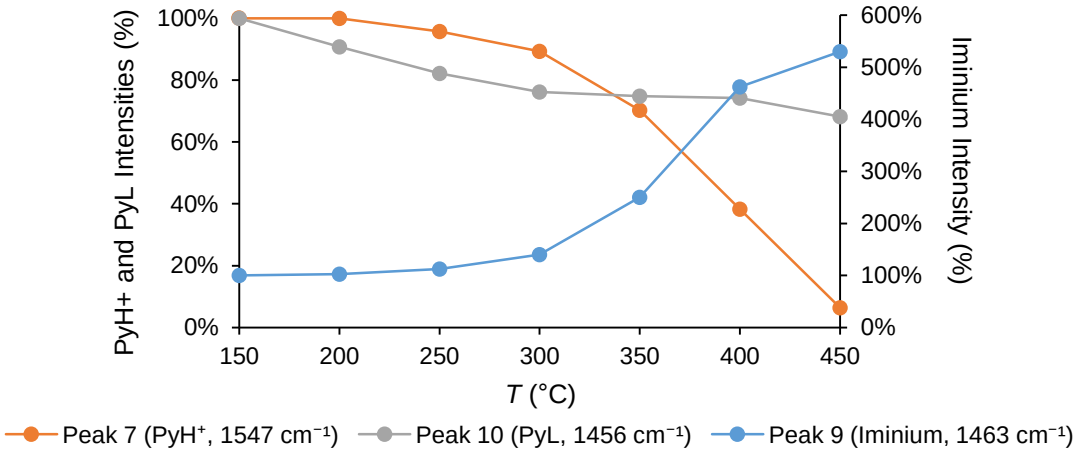

Figure 30 – Relative intensities of peaks 7, 9 and 10 in spectrum A (sample βOS)

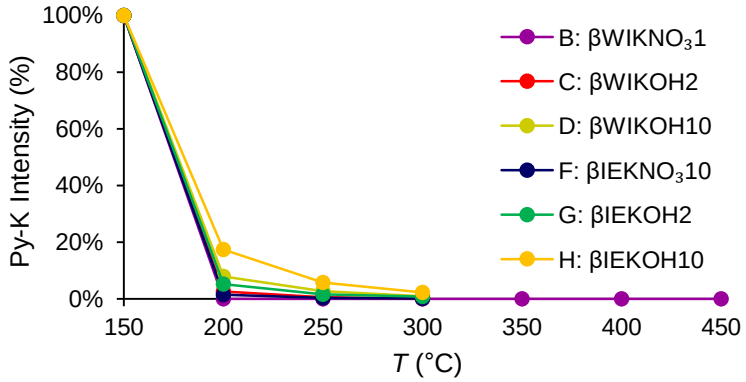

Figure 31 – Relative intensities of peak 12 (Py-K) in spectra B, C, D, F, G and H

BASICITY

The IR spectra of the eight calcined (at 500 °C for 4 hours) original and modified samples, collected post-activation at 30 °C, can be found below in Figure 32. These spectra were collected under vacuum after activation at 450 °C for 300 min (cf. Figure 14).

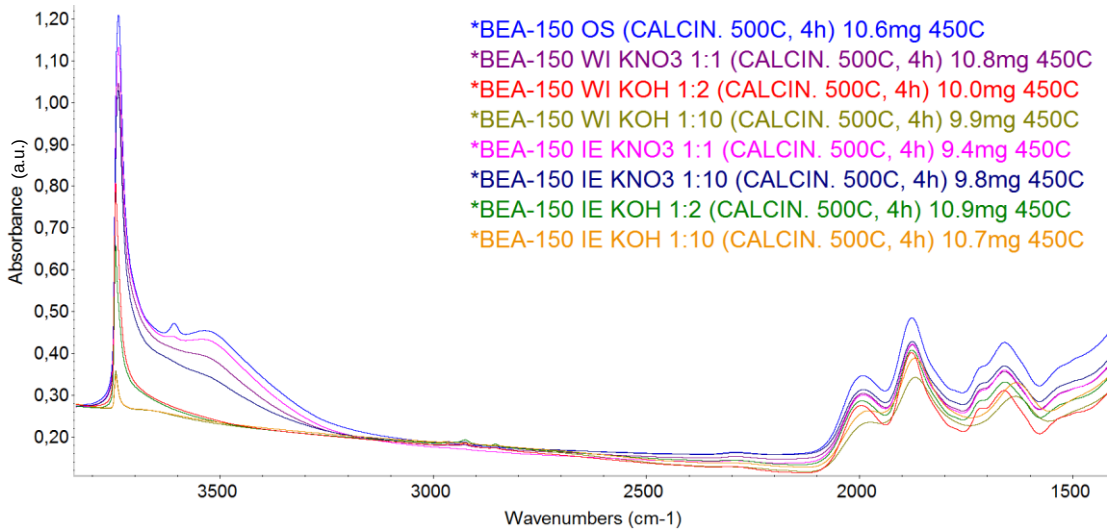

Figure 32 – IR spectra, collected at 30 °C, of the activated calcined original and modified BEA-150 samples

The spectra in Figure 32 follow the same trend in SiOH disappearance as the corresponding uncalcined samples' spectra in Figure 26, as was to be expected. However, the BAS band (3611 cm^{-1}) can now clearly be seen in the spectrum of sample βIEKNO$_3$1 ("BEA-150 IE KNO3 1:1") and it appears sharper for the spectrum of sample βOS ("BEA-150 OS"). This is a strong indication that there were indeed some contaminants associated with that frequency range that were obstructing the appearance of the BAS peak, that have now been removed by the calcination treatment. Furthermore, it can also be seen that the peaks at approximately 3000 – 2800 cm^{-1}, which are related to organic contaminants, have also decreased in comparison to those shown in Figure 26, having, likewise, been removed by calcination.

To study the basicity of the BEA-150 samples, acetylene (C_2H_2) was used as probe molecule. The adsorption spectra of this acidic probe molecule are shown in Figure 33. As previously done with pyridine, difference spectra were taken by subtracting each spectrum in Figure 33 by the corresponding activated sample's spectrum in Figure 32. The results can be found in Figure 34. Three peaks have been identified in the spectra in Figure 34 and summarised in Table 10.

Peaks 1 and 2 are associated with the asymmetrical C-H bond stretching frequency (gas phase, $\nu = 3287$ cm^{-1}) [50]. Peak 1, visible in spectra B and C, corresponds to a π-complex formed between the C≡C bond and the potassium cations, and represents a blueshift of the gas phase frequency [50]. As peak 1 is associated with the existence of potassium in the samples, it is not clear why it does not appear in the other potassium-containing samples' spectra. It is worth noting, however, that it appears solely in the spectra of impregnated samples, with the exception of spectrum D in which the sample has been almost completely destroyed by the 10-fold molar excess of KOH. Although unlikely, it could be suggested that the complex in peak 1 is related to external surface interactions, as in wet impregnation some precursor cations may be left in the external surface of the zeolite, unlike in ion exchange, where the exchanged cations tend to remain inside the pores. Peak 2, visible in all spectra, corresponds to an H-bond type connection with the framework basic oxygen, and represents a redshift of the gas phase frequency [50]. As basicity increases (i.e. potassium content in the sample) a slight redshift is noticeable in peak 2, which is due to bond weakening.

Peak 3 is associated with symmetrical C-C stretching frequencies ($\nu = 1974$ cm^{-1}) and should not, in theory, be seen in IR spectra. However, acetylene can adsorb unevenly onto the surface, causing a change in dipole moment, thus making symmetrical frequencies visible in the IR.

A small peak seen around 1700 cm^{-1} is associated with a minor acetone contamination.

Acetylene desorption was run first at RT (≈ 25 °C) and then following a TPD at 100 °C (cf. Figure 16). The latter was run to ensure a complete acetylene desorption, although in most samples this was achieved after the first desorption at RT. The nearly instant desorption of acetylene is an indicative of the expected weak bonding between the gaseous probe molecule and the solid support.

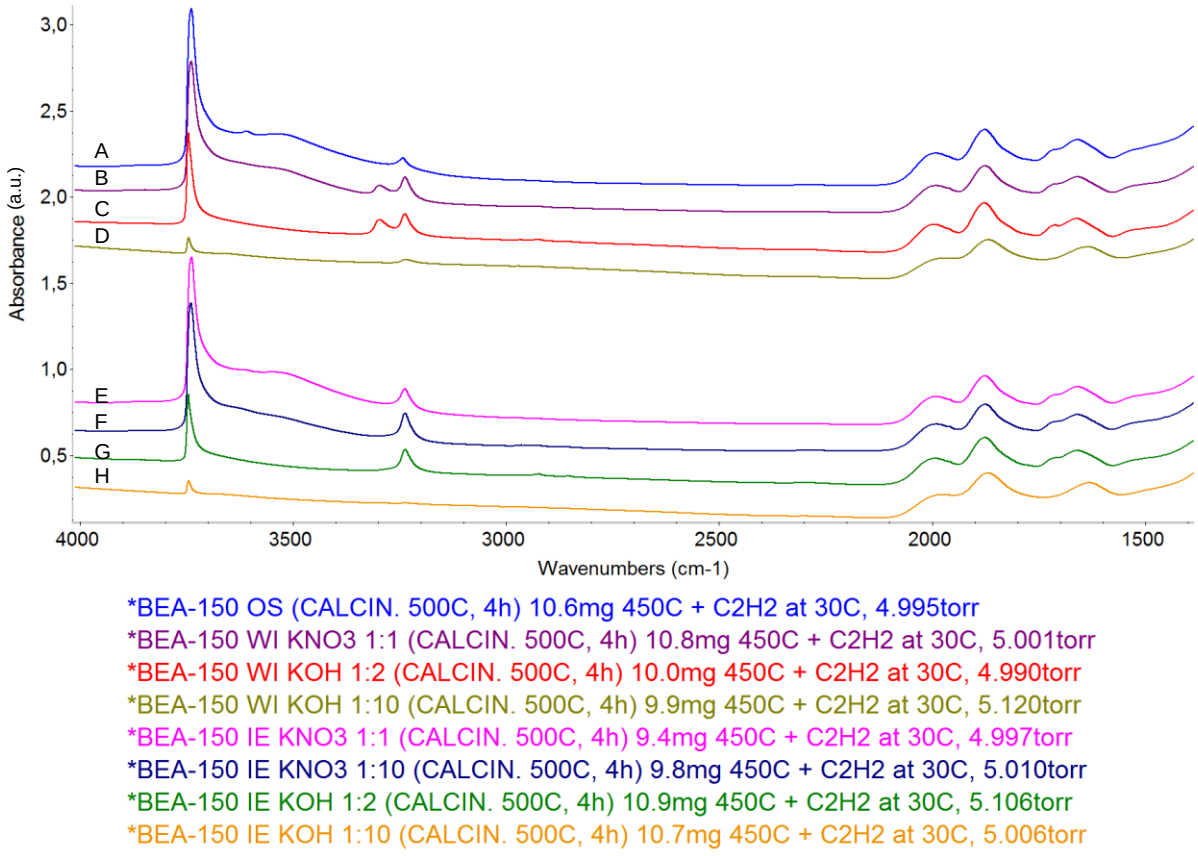

Figure 33 – IR spectra of the BEA-150 samples after acetylene adsorption at 30 °C and approximately 5 torr

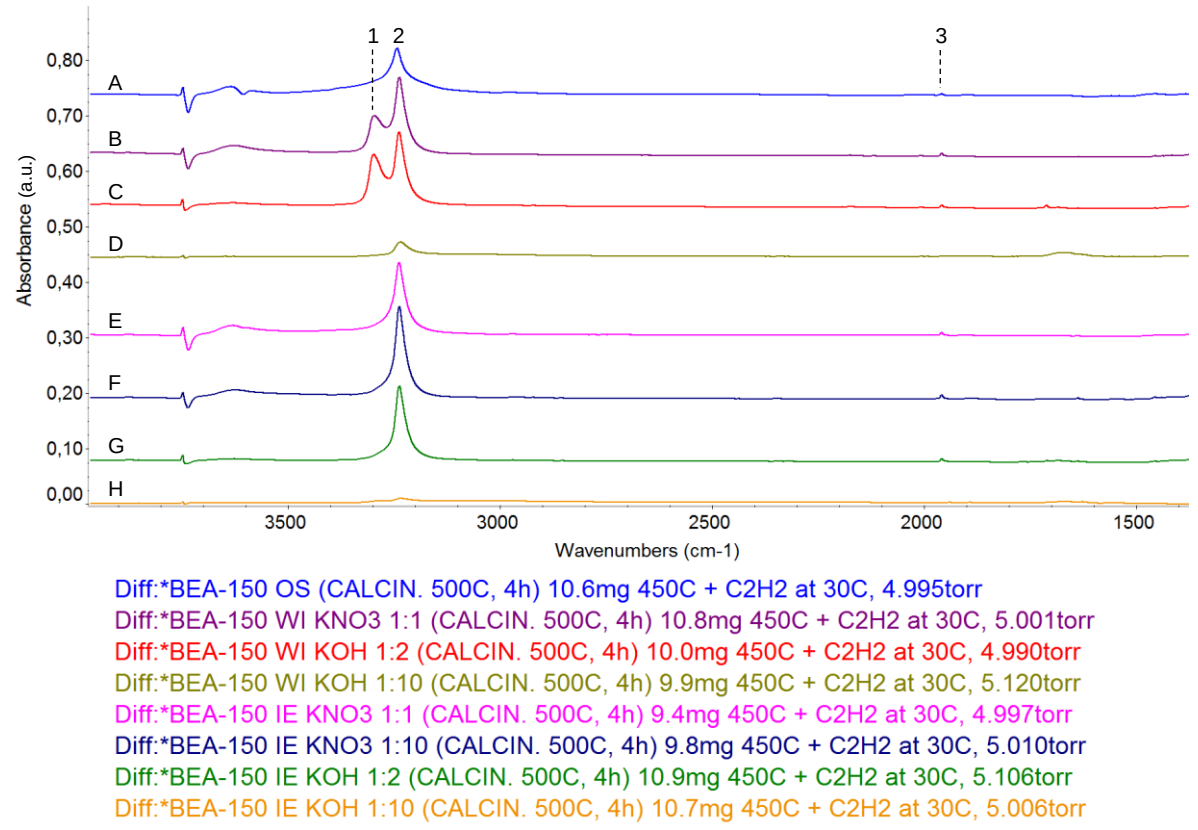

Figure 34 – Difference spectra of acetylene post-adsorption

Table 10 – Acetylene adsorption peaks

Peak	*v* (cm^{-1})	Spectra	Species
1	3298	B C	π-complex with K^+ (asymmetrical C-H stretching) [50]
2	3243 – 3236	A B C D E F G H	H-bond to framework O (asymmetrical C-H stretching) [50]
3	1959	A B C E F G	Symmetrical C-C bending

4.5. SORPTION EXPERIMENTS

N_2 sorption data is presented below. The MultiPoint BET plot was determined in the p/p_0 range of 0.02 – 0.1, which is lower than the common relative pressure range of linear applicability, 0.05 – 0.3 [40] [41] [42]. This is due to the samples being microporous, which shifts the linearity range to lower relative pressures [40] [42].

Figures 35 and 36 represent the N_2 sorption isotherms for the uncalcined and calcined samples, respectively. The isotherms obtained appear to be a combination of types I and IV: they present a high and steep incline for low relative pressures until circa 0.01, which is an indicative of the high amount of micropores in the structure of zeolite beta; from 0.01 until relative pressures of approximately 0.95 the multilayers are being adsorbed in larger pores (mesopores) until the zeolite's porous structure is entirely filled as N_2 capillary condensation occurs (final steep incline from p/p_0 of 0.95 to 1). The existence of hysteresis loops in all isotherms of the BEA-150 samples is an indicative of the existence of interparticle mesopores that could have been created by agglomeration of small crystallites [11]. The hysteresis loops, and therefore interparticle mesopores, increase for samples treated with KOH and, for those, with increasing potassium content, which is evidence of the gradual destruction of the structure by this strong base, as had been seen by experimental results already shown. Once again, it is also clear that the samples treated with a 10-fold molar excess of KOH have been almost completely destroyed; they present a much lower micropore volume and bigger hysteresis loops than the other samples. In Figure 36 it can also be seen that calcined samples appear to adsorb higher amounts of N_2, which is a result of the thermal treatment that removes impurities and moisture from the samples, increasing the available space for N_2 adsorption.

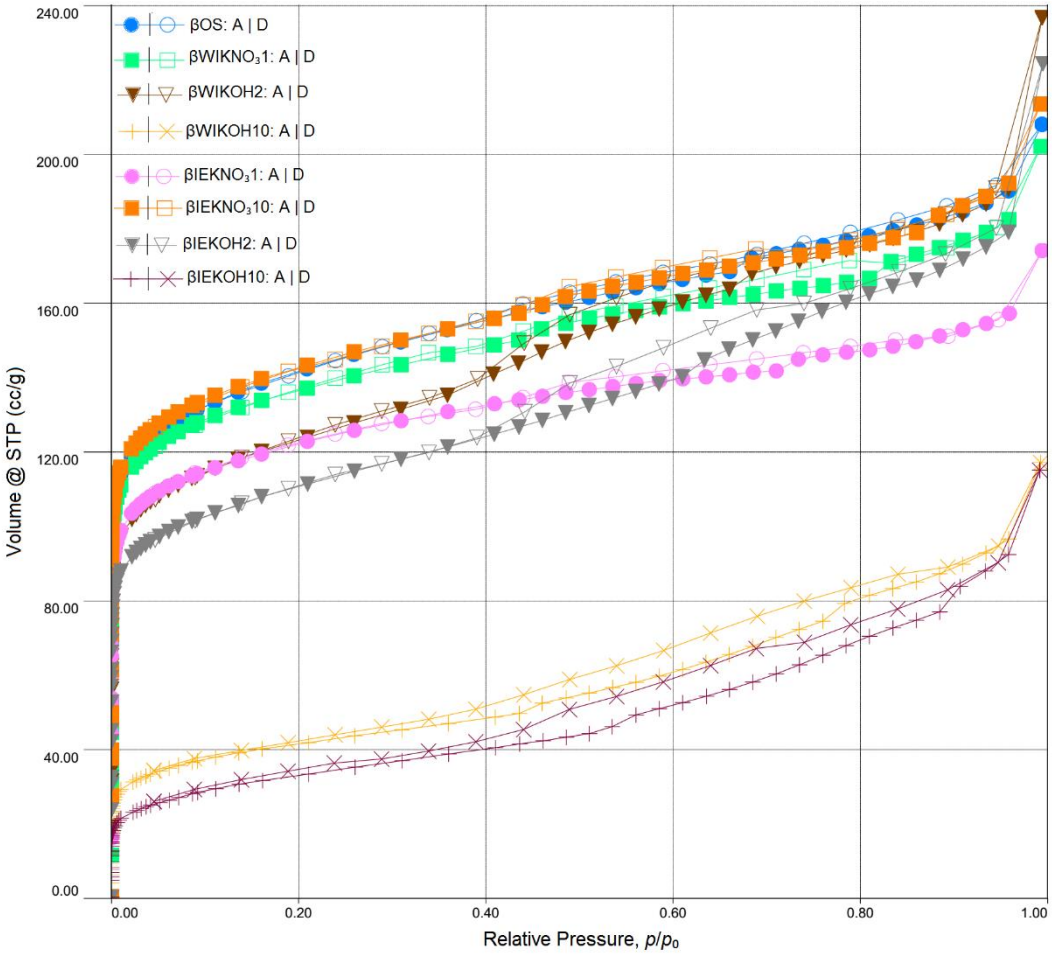

Figure 35 – N_2 sorption isotherms for the uncalcined BEA-150 samples

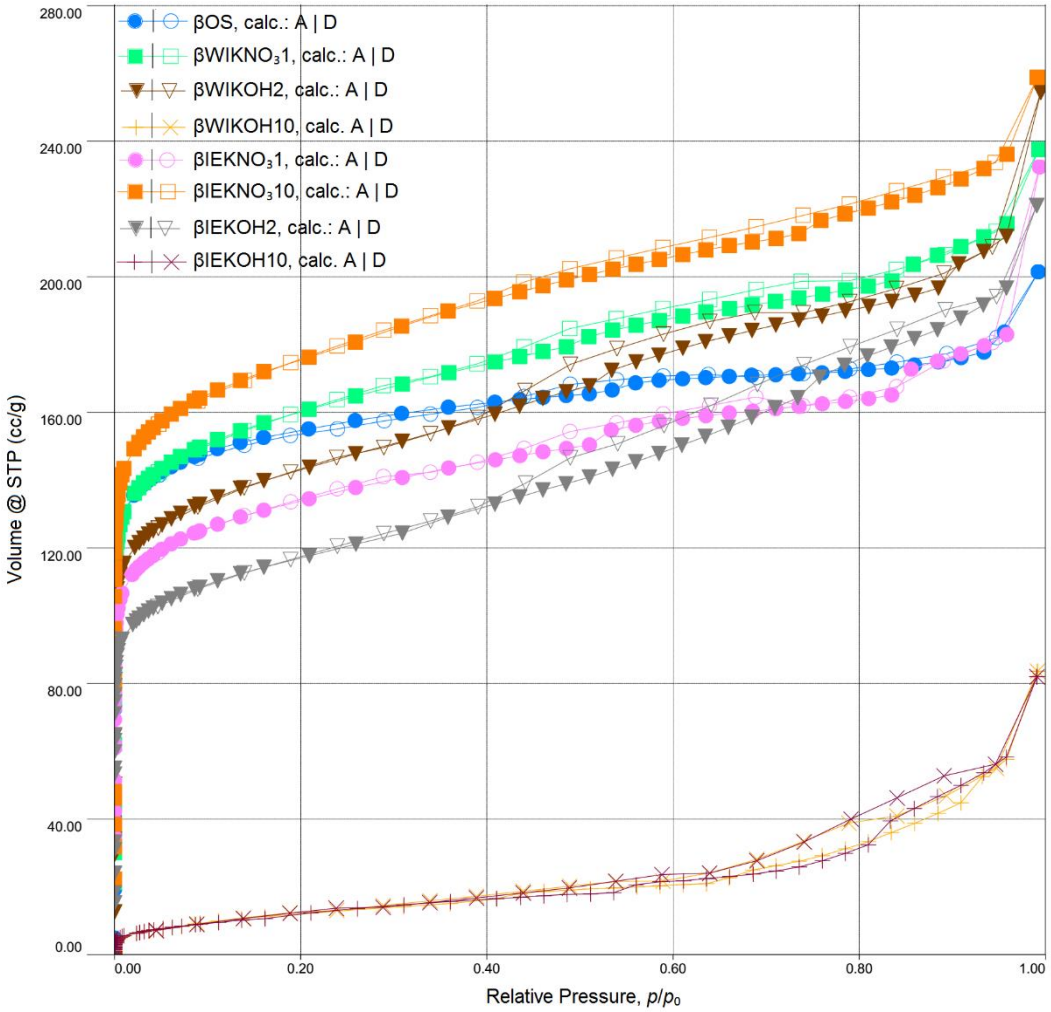

Figure 36 – N_2 sorption isotherms for the calcined BEA-150 samples

Surface area was calculated using the MultiPoint BET and *t*-plot (external and micropore surface areas) methods. The results can be found in Figure 37 for the uncalcined samples, in Figure 38 for the calcined samples and also in Tables C1 and C2 in Appendix C. The BET surface area for the original sample, βOS, is of the same order of magnitude as the value provided by the manufacturer (*Zeolyst International*, 620 m^2/g), and the difference may be attributed to variations in experimental setup and conditions. In general, BET surface area decreases with increasing potassium content, which would be expected considering that potassium, having a larger ionic radius than hydrogen, will occupy more space in the pores, hindering the progression and adsorption of N_2 molecules, thus resulting in lower BET surface areas. The exception to this trend is sample βIEKNO$_3$10, particularly the calcined form, which could be attributed to experimental error. It has also been suggested that the quadrupole moment of N_2 could be interacting with the potassium ions, resulting in its adsorption at different angles on the surface, thus increasing the overall adsorbed quantity [40]. This would not be the case with samples treated with KOH, which causes partial to severe structural damage and is conflicting with the suggestion that potassium hinders the progression and adsorption of N_2 into the pores. There may be a combination of these two suggestions happening with N_2 adsorption in potassium-containing samples.

For the uncalcined forms, it is possible to see that in the majority of samples the total surface area is approximately evenly split between external and micropore surface areas, as determined by the *t*-plot method, the exception being the samples treated with KOH with a K/Al molar ratio of 10, in which the micropore surface area consists of only a small percentage of the total surface area, as was to be expected, considering the collapse of micropores as a consequence of the destruction of these samples. After calcination, the micropore surface area appears to represent a bigger percentage of the total surface area, which was to be expected, due to the "cleansing" effect of calcination treatments, as mentioned earlier. For the calcined samples treated with a 10-fold molar excess of KOH, there is no micropore surface area detected by the *t*-plot method, which is another indicative of structural collapse. Lastly, and as expected, the results in Figures 37 and 38 show an increase in total surface area for the calcined samples in comparison with the uncalcined forms (e.g.: 588 m^2/g from 519 m^2/g for βOS), with the exception of the destroyed samples (e.g.: 38 m^2/g from 151 m^2/g for βWIKOH10).

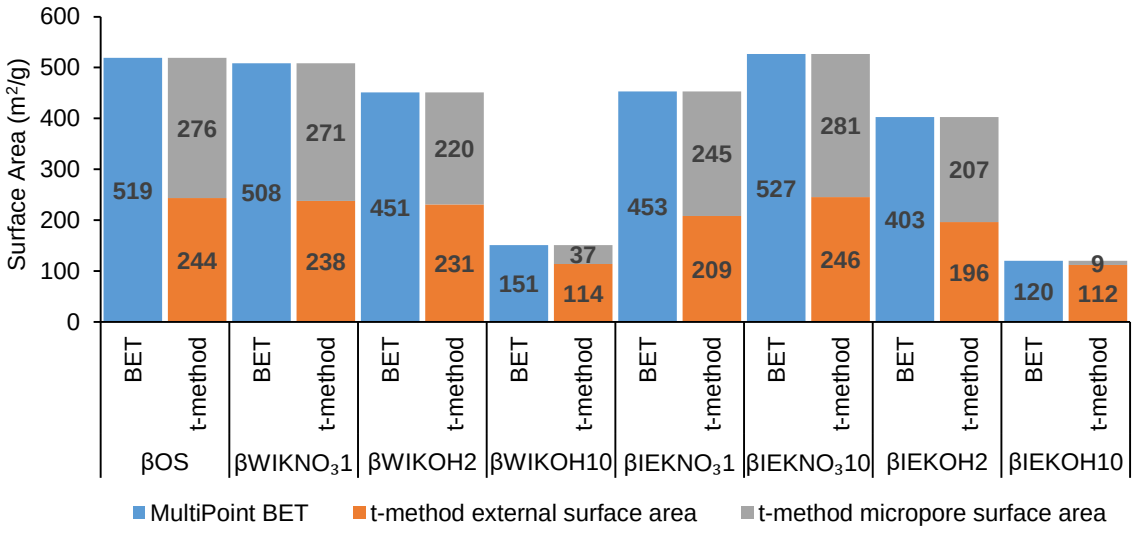

Figure 37 – MultiPoint BET and *t*-plot method (external and micropore) surface area for the uncalcined BEA-150 samples

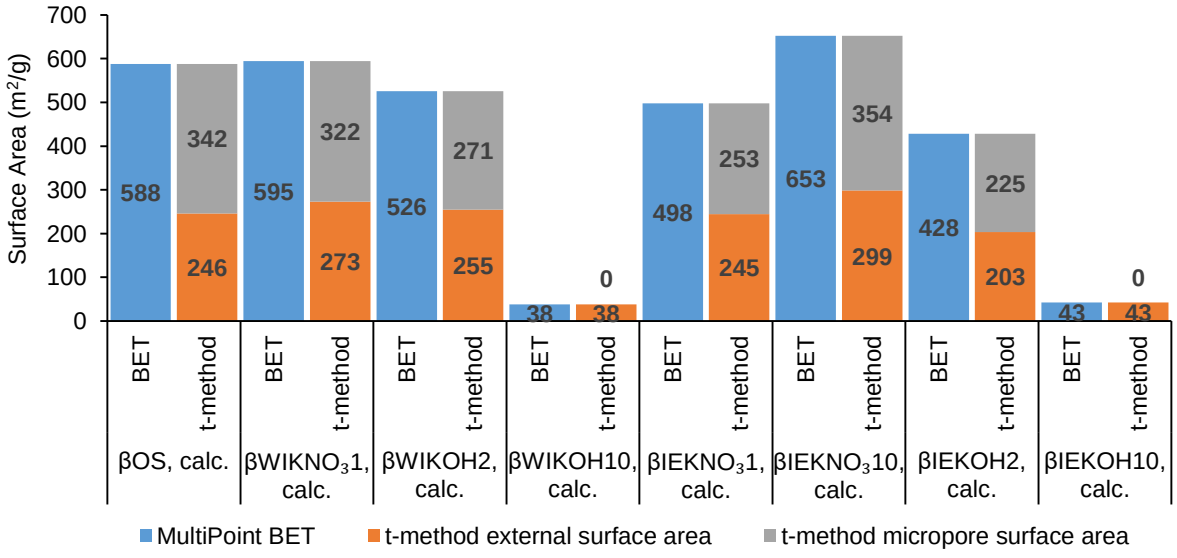

Figure 38 – MultiPoint BET and *t*-plot method (external and micropore) surface area for the calcined BEA-150 samples

Micropore volume has been calculated using the *t*-plot method and the results can be found in Figure 39 and also in Table C3 in Appendix C. The same trend in values for the calcined samples with respect to the uncalcined forms, and of the influence of potassium source and content, both seen previously, can be seen in Figure 39. The micropore volume is smaller, although in the same order of magnitude, than previously published results [22] [51], which is an indication that the zeolite beta used in this work is more mesoporous than those referenced.

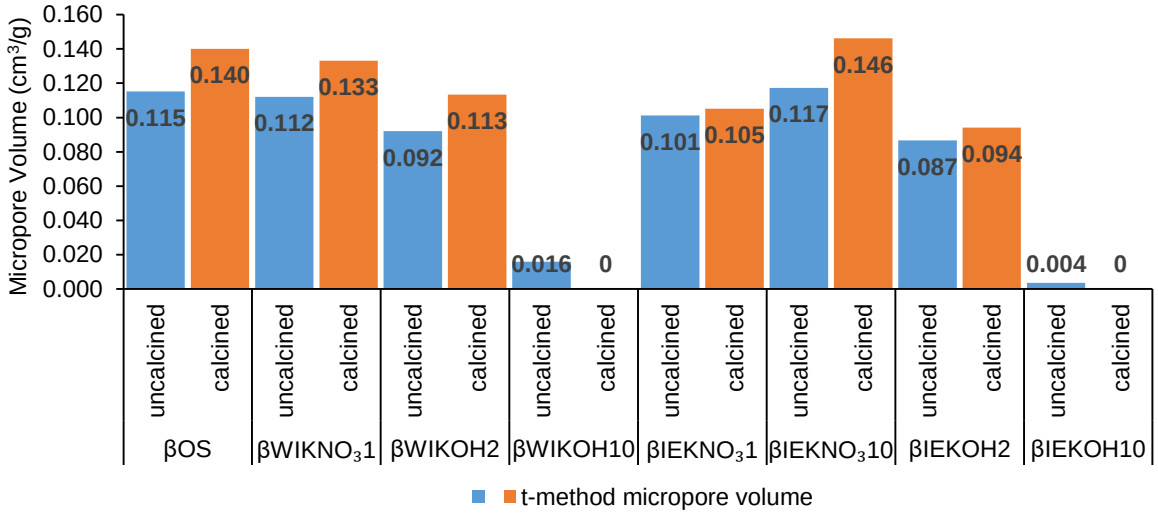

Figure 39 – *t*-plot method micropore volume for the uncalcined (■) and calcined (■) BEA-150 samples

DFT was run in the software (*Quantachrome ASiQwin 3.0)* to determine pore size distribution and diameter, using the parameters seen in Figure 40. Figures 41 and 42 display the pore size distribution in the range of 0 – 28 Å for the uncalcined and calcined samples, respectively. Figure 43 presents the pore diameter determined for all samples, also listed in Table C4 in Appendix C.

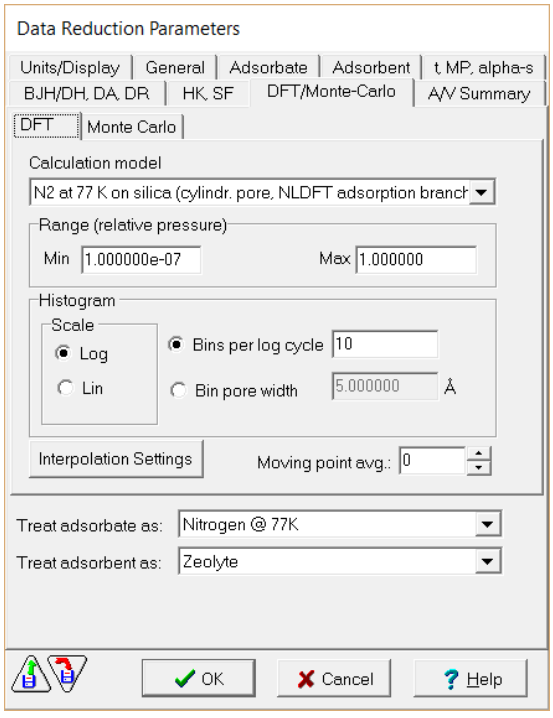

Figure 40 – Experimental DFT parameters used in the *Quantachrome ASiQwin 3.0* software

Figure 41 shows that the majority of the uncalcined samples have micropores of approximately 8 Å with a smaller amount of micropores of approximately 10 Å, whereas the pore size distribution for the calcined samples in Figure 42 shows that the majority of pores have a size of approximately 10 Å, which is a consequence of the calcination treatment, as mentioned before. Overall, pore size is in accordance with previously published values [21]. Once again the destroyed samples fall off this trend. This is particularly notable for the calcined destroyed samples as can be seen in the chart in Figure 43, where the DTF calculation has determined a pore size of 67.9 Å for sample βWIKOH10 (calc.) and 101.3 Å for sample βIEKOH10 (calc.).

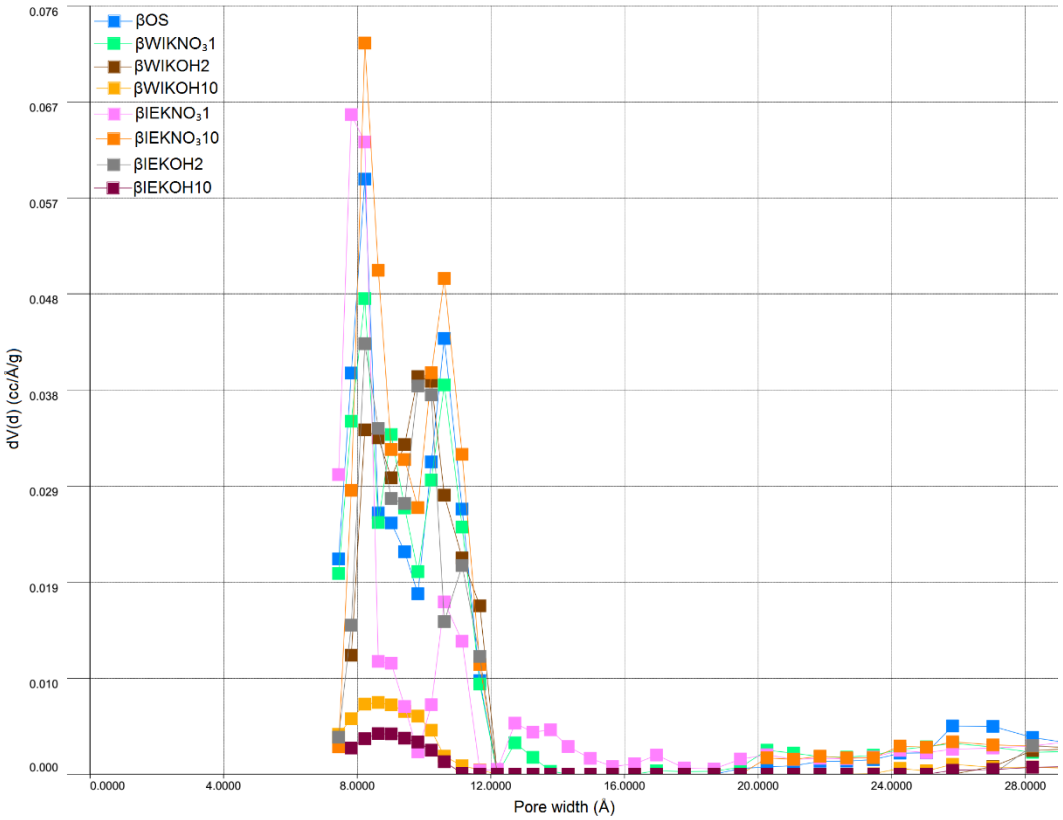

Figure 41 – DFT pore size distribution for the uncalcined BEA-150 samples

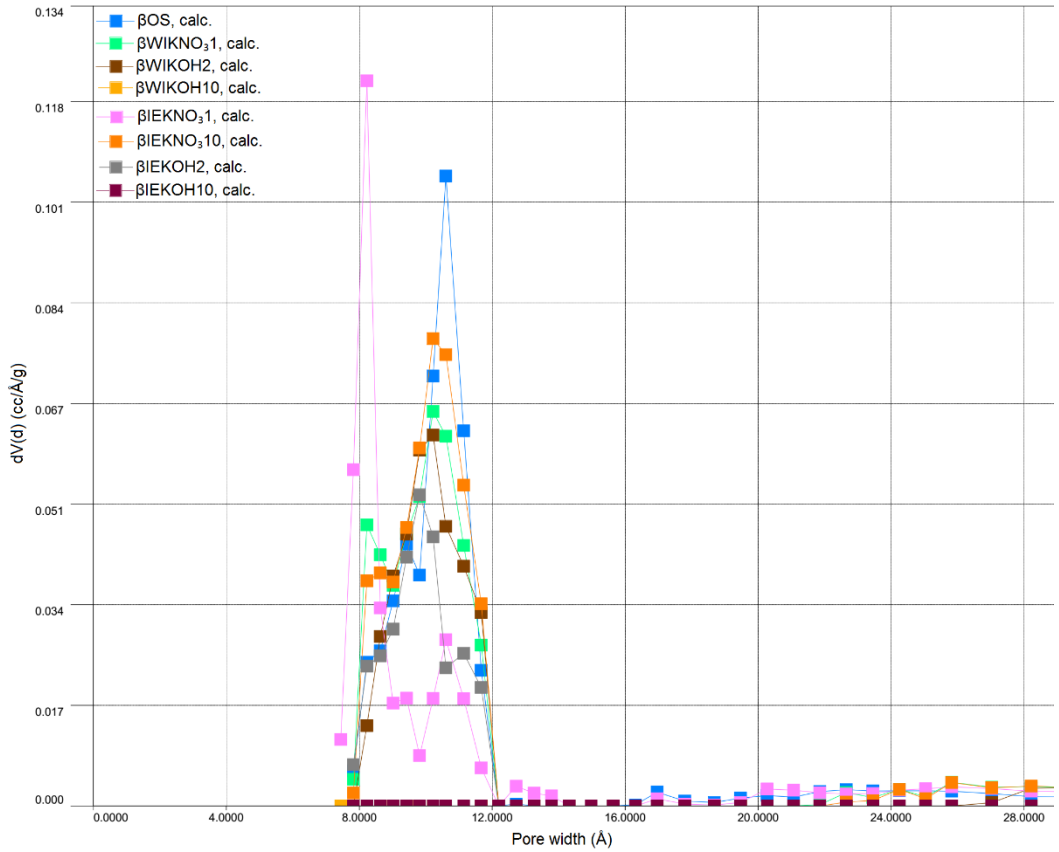

Figure 42 – DFT pore size distribution for the calcined BEA-150 samples

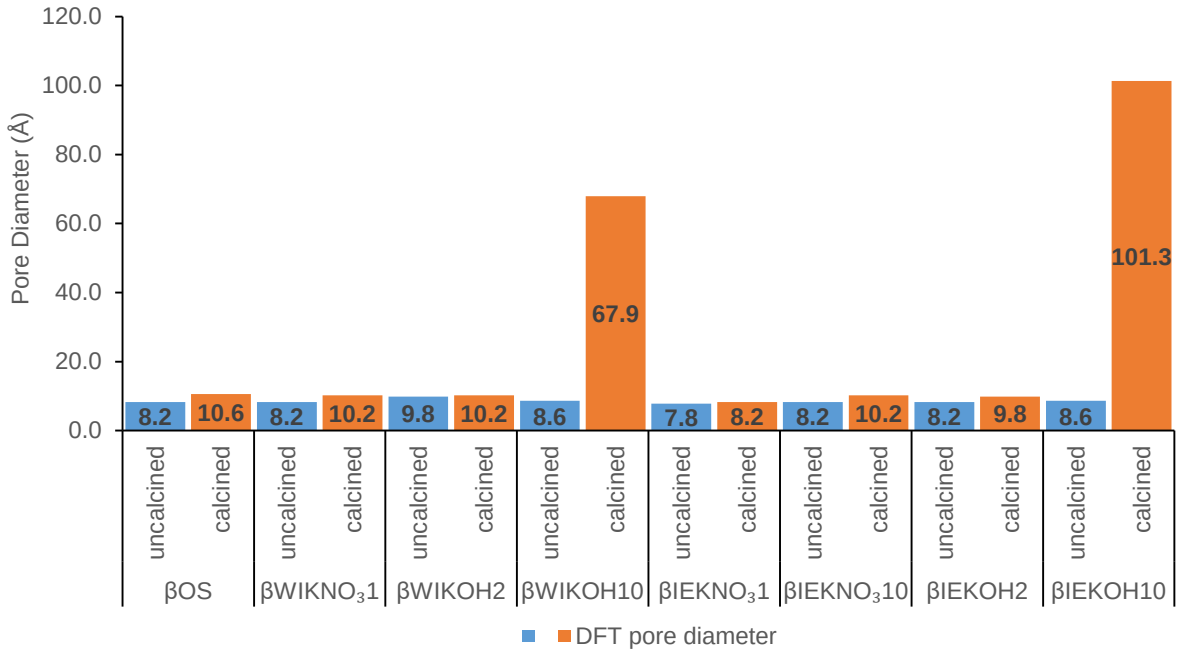

Figure 43 – DFT pore diameter for the uncalcined (■) and calcined (■) BEA-150 samples

5. CONCLUSION

The main objective of this work was to obtain a basic form of zeolite beta (BEA-150, Si/Al = 150) that could potentially be used as a basic heterogeneous catalyst for biodiesel production. This work was part of an ongoing project on the subject of biodiesel production, which also involves other researchers, and was developed in the Birchall Centre at Keele University. It consisted of the post-synthesis modification and characterisation of eight different samples of zeolite BEA-150.

Zeolite beta is a highly disordered microporous structure with 12-membered ring pores and an inner system of channels and cavities that are particularly tortuous in the c direction. BEA-150 would be expected to have an acidic nature, on account of being in its protonic form and its low aluminium content.

The modifications performed in BEA-150 were achieved by the employment of the post-synthesis modification techniques of wet impregnation and ion exchange, that introduced potassium cations as the charge-compensating extra-framework cations in the protonic form of BEA-150, obtained from *Zeolyst International*, thus increasing its basicity.

Initially, six samples were prepared: three for wet impregnation and three for ion exchange. The sources for potassium were aqueous solutions of KNO_3 (K/Al = 1) and KOH (K/Al = 2, 10) prepared *in situ*. Initial characterisation by SEM/EDS showed that the molar Si/Al ratios for all samples (including the original, unmodified BEA-150) were approximately half of the expected values, although consistent within themselves. The same result was found for the K/Al ratios for the modified samples, although in this case, ion exchanged samples were not expected to have a K/Al molar ratio higher than 1 (as per the definition of this technique). For the sample modified by ion exchange with KOH and a K/Al molar ratio of 10, EDS analysis showed an experimental K/Al molar ratio of 5. To determine the source of this discrepancy, an additional sample was modified by ion exchange with a K/Al molar ratio of 10, this time using KNO_3 as the alkali metal precursor. SEM/EDS analysis performed on this sample gave a K/Al molar ratio below 1, as was to be expected, and a Si/Al molar ratio of approximately half of the anticipated 150, which was consistent with the previous samples' results. The phenomenon of the halved Si/Al and K/Al molar ratios obtained for the samples was attributed to the detection limit of the SEM/EDS equipment being insufficient to determine such low amounts of aluminium. This was confirmed by the testing of two unrelated samples of ZSM-5 (Si/Al = 40) and BEA-19 (Si/Al = 19), whose Si/Al ratios obtained by the same SEM/EDS equipment were close to their expected values, within an acceptable margin of error.

XRD was performed to determine the crystalline structure of the eight BEA-150 samples (original and modified) and it was found that the samples treated with a 10-fold molar excess of KOH showed a significant loss of crystal structure, which indicated that the large excess used of this strong base destroyed the zeolite framework, by causing desilication in the structure. This was not the case with the seventh additional ion exchange sample prepared, because KNO_3 is an ionic salt with an almost neutral pH. Furthermore, all samples treated with KNO_3 presented greater crystallinities, relative to the original unmodified sample. This was attributed to the stronger scattering effect of X-rays by potassium, in comparison to hydrogen.

It was suggested that calcination would improve the catalytic performance of the samples, and as such, the eight samples were calcined at 500 °C for a period of 4 hours. XRD patterns obtained for these calcined samples showed an improvement in the crystallinity in comparison to the uncalcined forms, as was to be expected, given that calcination removes contaminants and moisture from the structure, which improves the contrast on the samples scanned by the XRD instrument, resulting in sharper peaks in the patterns. The exception to this were the samples treated with a 10-fold molar excess of KOH, which had suffered desilication and now underwent dealumination as a result of the thermal treatment, further disintegrating these samples' structures.

FTIR was performed to evaluate the acidity and basicity of the samples; pyridine (Py) was used as probe molecule to assess the acidity of the uncalcined samples and acetylene (C_2H_2) was used to assess the basicity of the calcined samples. In both cases, TPD was run to measure the desorption of the probe molecules from the active sites. The spectra collected in all samples showed a considerable decrease in the silanol IR band with the increasing strength and content of the potassium source. These results showed KOH not only reacted with hydrogen containing BAS (Si-O(H)-Al) but had also aggressively reacted with silanol groups, causing desilication that resulted in structure collapse. This was concluded to be the reason as to why the initial K/Al molar ratio obtained by SEM/EDS for the samples modified by ion exchange with KOH was much higher than 1. IR spectra also showed the existence of a small amount of BAS and silanol nests at their respective characteristic IR bands. Upon pyridine adsorption, the typical peaks for pyridine interactions were observed in the range of 1700 – 1400 cm^{-1}, the most notable being PyH^+ (from BAS, 1547 cm^{-1}) and PyL (from LAS, 1456 cm^{-1}) and for the modified samples Py-K (from physisorption to potassium, 1443 – 1441 cm^{-1}). The PyL peak at 1456 cm^{-1} is mostly associated with EFAL species and only appeared in the spectra of the original sample and the sample treated by ion exchange with KNO_3 and a K/Al molar ratio of 1. This is an indicative that there weren't many EFAL species in the samples and that they were most likely removed with the aqueous solutions used in the modifications. Py-TPD on the original sample showed the formation of a new species, iminium ions, which are the result of a protonic attack to PyL centres. The formation of these iminium ions was mirrored by the desorption of pyridine from BAS, and both increased and decreased, respectively, much faster from 300 ºC onwards. Pyridine was almost completely removed from BAS, indicating the strong acidic nature of these sites; the desorption from LAS was steady and incomplete, which is suggestive of the very strong nature of these sites. Desorption from potassium was complete and almost instantaneous. C_2H_2 adsorption to the calcined samples revealed two major peaks in the range of 3300 – 3200 cm^{-1}, associated with the asymmetrical C-H stretching frequency. The higher frequency peak (detected at 3298 cm^{-1}) is associated with a π-complex formed between the triple C≡C bond and potassium cations. This peak was only detected in impregnated samples that were not already destroyed and although unlikely, it may be related to external surface interactions. The lower frequency peak (detected in the range of 3243 – 3236 cm^{-1}) corresponds to a hydrogen bond with the framework basic oxygens, and the more basic the sample is, the more the peak shifts to lower frequencies. C_2H_2 desorption from both sites was, in most samples, instantaneous at 25 ºC.

Lastly, N_2 sorption experiments were run in all sixteen samples. Surface area was calculated using MultiPoint BET and *t*-plot method (for external and micropore surface areas). Micropore volume was calculated using *t*-plot method and pore size distribution and diameter were determined by DFT.

The isotherms obtained for all samples revealed an intermediate character between types I and IV isotherms: significant micropore volume, existence of interparticular mesopores and N_2 capillary condensation. Overall, calcined samples showed better N_2 adsorption than the uncalcined forms, which was attributed to the removal of contaminants and moisture from the structure by this thermal treatment. Potassium was suggested to be hindering N_2 adsorption, due to its larger size when compared to hydrogen. The experimental surface area(s), micropore volume and pore size are in the same order of magnitude as previously published results.

The overall results have shown that basicity has been achieved, and that to a certain extent KOH is a more effective basicity inducing precursor than KNO_3. Wet impregnation was found to be more effective for exchanged cation retention than ion exchange.

It should be noted that careful consideration should always be taken in the choice of characterisation techniques, and their operating parameters. Often, spectroscopic techniques have certain limitations and results can be deceiving, until the employment of different techniques sheds further light on the overall results. The combination of different characterisation techniques allows for a much more complete and precise assessment of the properties of a single (or set of) sample(s).

Pyridine and acetylene have proven to be good probe molecules to assess the acidity and basicity of the samples. N_2 has also proven to be a good adsorptive gas, although ideally a monoatomic gas like argon should be used to prevent unevenly surface adsorption.

Future work should now be conducted to further characterise the active sites, by determining their exact amount and location. As an example, thermogravimetric analysis (TGA) could be employed to determine the concentration of catalytic sites and smaller (or bigger) IR molecular probes could be used to distinguish between sites in differently sized pores.

Nowadays more importance is being given to hierarchical zeolites, and that is mostly due to their exceptional versatile nature. The experimental results have shown that there are some mesopores in an otherwise microporous structure of the samples. These mesopores may have been created by desilication and dealumination phenomena or by agglomeration of smaller crystallites. Further research should be taken to implement the development of hierarchical BEA-150 zeolites.

Since zeolite BEA-150 was obtained commercially, another zeolite-type material, ETS-10, was synthesised outside the scope of this work for educational and scientific purposes. The synthesis steps and results have not been included in this work. ETS-10 is a titanosilicate with a good potential as basic heterogeneous catalyst for biodiesel production.

On a final note, catalytic tests of biodiesel production (through transesterification with excess methanol) have been performed outside the scope of this work. The results have shown that the destroyed samples gave the highest conversions. However, this has been attributed to homogeneous catalysis, given the degree of structural damage. In this case, catalyst regeneration was unsuccessful.

REFERENCES

[1] M. R. Avhad and J. M. Marchetti, “A review on recent advancement in catalytic materials for biodiesel production,” *Renewable and Sustainable Energy Reviews,* vol. 50, pp. 696-718, 2015.

[2] M. R. Avhad and J. M. Marchetti, “Innovation in solid heterogeneous catalysis for the generation of economically viable and ecofriendly biodiesel: A review,” *Catalysis Reviews,* vol. 58:2, pp. 157-208, 2016.

[3] M. K. Lam, K. T. Lee and A. R. Mohamed, “Homogeneous, heterogeneous and enzymatic catalysis for transesterification of high free fatty acid oil (waste cooking oil) to biodiesel: A review,” *Biotechnology Advances,* vol. 28, pp. 500-518, 2010.

[4] D. W. Lee, Y. M. Park and K. Y. Lee, “Heterogeneous Base Catalysts for Transesterification in Biodiesel Synthesis,” *Catalysis Surveys from Asia,* vol. 13, pp. 63-77, 2009.

[5] Zion Research Analysis, December 2015. [Online]. Available: http://www.marketresearchstore.com/report/zeolite-market-z41101. [Accessed August 2016].

[6] H. van Bekkum, E. M. Flanigen, P. A. Jacobs and J. C. Jansen, Eds., Introduction to Zeolite Science and Practice, Second ed., Amsterdam, The Netherlands: Elsevier, 2001.

[7] W. Loewenstein, “The distribution of aluminium in the tetrahedra of silicates and aluminates,” *American Mineralogist,* vol. 39, pp. 92-96, 1954.

[8] International Zeolite Association, “IZA Structure Comission,” [Online]. Available: http://www.iza-structure.org/default.htm. [Accessed October 2016].

[9] International Zeolite Association, “IZA Comission on Natural Zeolites,” [Online]. Available: http://www.iza-online.org/natural/default.htm. [Accessed August 2016].

[10] K. Margeta, N. Z. Logar, M. Šiljeg and A. Farkas, “Natural Zeolites in Water Treatment – How Effective is Their Use,” 2013. [Online]. Available: http://www.intechopen.com/books/water-treatment/natural-zeolites-in-water-treatment-how-effective-is-their-use. [Accessed June 2016].

[11] M. Guisnet and F. Râmoa Ribeiro, Zeólitos: Um Nanomundo ao Serviço da Catálise, Lisbon, Portugal: Fundação Calouste Gulbenkian, 2004.

[12] C. Baerlocher, L. B. McCusker and D. Olson, The Atlas of Zeolite Framework Types, Sixth ed., Amsterdam, The Netherlands: Elsevier, 2007.

[13] A. Corma and A. Martínez, “The Chemistry of Catalytic Processes,” in *Zeolites for Cleaner Technologies*, M. Guisnet and J. Gilson, Eds., London, United Kingdom, Imperial College Press, 2002, pp. 29-55.

[14] E. G. Derouane, J. C. Védrine, R. Ramos Pinto, P. M. Borges, L. Costa, M. A. N. D. A. Lemos, F. Lemos and F. Ramôa Ribeiro, “The Acidity of Zeolites: Concepts, Measurements and Relation to Catalysis: A Review on Experimental and Theoretical Methods for the Study of Zeolite Acidity,” *Catalysis Reviews,* vol. 55:4, pp. 454-515, 2013.

[15] M. Boronat and A. Corma, “Factors Controlling the Acidity of Zeolites,” *Catalysis Letters,* vol. 145:1, pp. 162-172, 2015.

[16] J. Weitkamp and M. Hunger, “Acid and Base Catalysis on Zeolites,” in *Studies in Surface Science and Catalysis: Introduction to Zeolite Science and Practice (3rd Revised Edition)*, vol.

168, J. Čejka, H. van Bekkum, A. Corma and F. Schüth, Eds., Amsterdam, The Netherlands, Elsevier, 2007, pp. 787-835.

[17] S. Bordiga, C. Lamberti, F. Bonino, A. Travert and F. Thibault-Starzyk, “Probing zeolites by vibrational spectroscopies,” *Chemical Society Review,* vol. 44, pp. 7262-7341, 2015.

[18] Y. Ono and H. Hattori, Solid Base Catalysis, Berlin, Germany; Tokyo, Japan: Springer; Tokyo Institute of Technology Press, 2011.

[19] J. Zhu, Y. Chun, Y. Wang and Q. Xu, “Preparing strong basic zeolite molecular sieve catalytic materials,” *Chinese Science Bulletin,* vol. 44:21, pp. 1926-1934, 1999.

[20] R. L. Wadlinger, G. T. Kerr and E. J. Rosinski, “Catalytic Composition of a Crystalline Zeolite”. New York, United States of America Patent US3308069, 7 March 1967.

[21] J. B. Higgins, R. B. LaPierre, J. L. Schlenker, A. Rohrman, J. Wood, G. Kerr and W. J. Rohrbaugh, “The framework topology of zeolite beta,” *Zeolites,* vol. 8:6, pp. 446-452, 1988.

[22] J. M. Newsam, M. J. Treacy and W. T. Koetsier, “Structural Characterization of Zeolite Beta,” *Proceedings of the Royal Society of London A,* vol. 420, pp. 375-405, 1988.

[23] K. Shanjiao, G. Yanjun, D. Tao, Z. Ying and Z. Yanying, “Preparation and Characterization of Zeolite Beta with Low SiO2/Al203 Ratio,” *Petroleum Science,* vol. 4:1, pp. 70-74, 2007.

[24] J. P. Marques, I. Gener, P. Ayrault, J. C. Bordado, J. M. Lopes, F. Râmoa Ribeiro and M. Guisnet, “Infrared spectroscopic study of the acid properties of dealuminated BEA zeolites,” *Microporous and Mesoporous Materials,* vol. 60, pp. 251-262, 2003.

[25] M. Tong, D. Zhang, W. Fan, J. Xu, L. Zhu, W. Guo, W. Yan, J. Yu, S. Qiu, J. Wang, F. Deng and R. Xu, “Synthesis of chiral polymorph A-enriched zeolite Beta with an extremely concentrated fluoride route,” *Nature: Scientific Reports,* vol. 5:11521, 2015.

[26] International Zeolite Association, “Framework Type *BEA,” [Online]. Available: http://rcsr.fos.su.se/IZA-SC/ftc_fw.php?STC=BEA. [Accessed June 2016].

[27] A. Simon-Masseron, J. P. Marques, J. M. Lopes, F. Ramôa Ribeiro, I. Gener and M. Guisnet, “Influence of the Si/Al ratio and crystal size on the acidity and activity of HBEA zeolites,” *Applied Catalysis A: General,* vol. 316, pp. 75-82, 2007.

[28] Y. Wang, D. Lee and B. Chen, “Low-Al Zeolite Beta as a Heterogeneous Catalyst in Biodiesel Production from Microwave-assisted Transesterification of Triglycerides,” *Energy Procedia,* vol. 6, pp. 918-921, 2014.

[29] Q. Zhang, W. Ming, J. Ma, J. Zhang, W. P. and R. Li, “De novo assembly of a mesoporous beta zeolite with intracrystalline channels and its catalytic performance for biodiesel production,” *Journal of Materials Chemistry A,* vol. 2, pp. 8712-8718, 2014.

[30] E. Marceau, X. Carrier, M. Che, O. Clause and C. Mrcilly, “Ion Exchange and Impregnation,” in *Handbook of Heterogeneous Catalysis*, Second ed., vol. 1, G. Ertl, H. Knözinger, F. Schüth and J. Weitkamp, Eds., Weinheim, Germany, Wiley, 2008, pp. 467-484.

[31] J. Goldstein, D. E. Newbury, D. C. Joy, C. E. Lyman, P. Echlin, E. Lifshin, L. Sawyer and J. R. Michael, Scanning Electron Microscopy and X-ray Microanalysis, Third Edition ed., New York, USA: Springer, 2003.

[32] A. W. Burton, “Powder Diffraction in Zeolite Science: An Introductory Guide,” in *Zeolite Characterization and Catalysis: A Tutorial*, A. W. Chester and E. G. Derouane, Eds., New York, USA, Springer, 2009, pp. 1-64.

[33] R. E. Morris and P. S. Wheatley, “Diffraction Techniques Applied to Zeolites,” in *Studies in Surface Science and Catalysis: Introduction to Zeolite Science and Practice (3rd Revised Edition)*, vol. 168, J. Čejka, H. van Bekkum, A. Corma and F. Schüth, Eds., Amsterdam, The Netherlands, Elsevier, 2007, pp. 375-401.

[34] Australian Microscopy & Microanalysis Research Facility, “MyScope: X-ray diffractometer,” [Online]. Available: http://li155-94.members.linode.com/myscope/xrd/background/machine/. [Accessed November 2016].

[35] X. Liu, “Infrared and Raman Spectroscopy,” in *Zeolite Characterization and Catalysis: A Tutorial*, A. W. Chester and E. R. Derouane, Eds., New York, USA, Springer, 2009, pp. 197-222.

[36] B. C. Smith, Fundamentals of Fourier Transform Infrared Spectroscopy, Second Edition ed., Boca Raton, Florida, USA: CRC Press, 2011.

[37] F. Thibault-Starzyk and F. Maugé, “Infrared Spectroscopy,” in *Characterization of Solid Materials and Heterogeneous Catalysts: From Structure to Surface Reactivity*, vol. 1, M. Che and J. C. Védrine, Eds., Weinheim, Germany, Wiley-VCH, 2012, pp. 3-48.

[38] B. C. Smith, Infrared Spectral Interpretation: A Systematic Approach, Boca Raton, Florida, USA: CRC Press, 1999.

[39] A. Fernandes, J. M. Lopes and R. Ramos Pinto, “Characterization of Acid Catalysts,” in *Catalysis from Theory to Application: An Integrated Course*, J. L. Figueiredo, M. M. Pereira and J. Faria, Eds., Coimbra, Portugal, Imprensa da Universidade de Coimbra, 2008, pp. 145-165.

[40] P. L. Llewellyn, E. Bloch and S. Bourrelly, “Surface Area/Porosity, Adsorption, Diffusion,” in *Characterization of Solid Materials and Heterogeneous Catalysts: From Structure to Surface Reactivity*, vol. 1, M. Che and J. C. Védrine, Eds., Weinheim, Germany, Wiley-VCH, 2012, pp. 853-879.

[41] K. S. W. Sing, D. H. Everett, R. A. W. Haul, L. Moscou, R. A. Pierotti, J. Rouquerol and T. Siemieniewska, “Reporting Physisorption Data for Gas/Solid Systems,” in *Handbook of Heterogeneous Catalysis (Second, Completely Revised and Enlarged Edition)*, vol. 1, G. Ertl, H. Knözinger, F. Schüth and J. Wetikamp, Eds., Weiheim, Germany, Wiley-VCH, 2008, pp. 1217-1230.

[42] International Organization for Standardization, “Determination of the specific surface area of solids by gas adsorption - BET method,” ISO 9277:2010, Geneva, Switzerland, 2010-09-01.

[43] M. Hunger, “Solid-State NMR Spectroscopy,” in *Zeolite Characterization and Catalysis: A Tutorial*, A. W. Chester and E. G. Derouane, Eds., New York, USA, Springer, 2009, pp. 65-105.

[44] International Zeolite Association, “Catalog of Disordered Zeoltie Structures: The Beta Family”.

[45] D. P. Serrano, J. M. Escola and P. Pizarro, “Synthesis strategies in the search for hierarchical zeolites,” *Chemical Society Reviews,* vol. 42, pp. 4004-4035, 2013.

[46] K. Li, J. Valla and J. Garcia-Martinez, “Realizing the Commercial Potential of Hierarchical Zeolites: New Opportunities in Catalytic Cracking,” *ChemCatChem,* vol. 6:1, pp. 46-66, 2014.

[47] J. Datka, K. Tarach and K. Góra-Marek, “Acidic Properties of Hierarchical Zeolites,” in *Mesoporous Zeolites: Preparation, Characterization and Applications*, J. García-Martínez and K. Li, Eds., Weinheim, Germany, Wiley-VCH, 2015, pp. 461-496.

[48] M. Guisnet, P. Ayrault, C. Coutanceau, M. F. Alvarez and J. Datka, “Acid properties of dealuminated beta zeolites studied by IR spectroscopy,” *Journal of the Chemical Society, Faraday Transactions,* vol. 93:8, pp. 1661-1665, 1997.

[49] J. A. Lercher and A. Jentys, “Infrared and Raman Spectroscopy for Characterizing Zeolites,” in *Studies in Surface Science and Catalysis: Introduction to Zeolite Science and Practice (3rd Revised Edition)*, vol. 168, J. Čejka, H. van Bekkum, A. Corma and F. Schüth, Eds., Amsterdam, The Netherlands, Elsevier, 2007, pp. 435-476.

[50] E. B. Uvarova, L. M. Kustov and V. B. Kazansky, “Basicity of zeolites: IR-spectroscopic study using adsorbed molecular probes,” in *Studies in Surface Science and Catalysis: Catalysis by Microporous Materials, Proceedings of ZEOCAT '95*, vol. 94, H. K. Beyer, H. G. Karge, I. Kiricsi and J. B. Nagy, Eds., Amsterdam, The Netherlands, Elsevier, 1995, pp. 254-261.

[51] M. A. Camblor, A. Corma and S. Valencia, “Characterization of nanocrystalline zeolite Beta,” *Microporous and Mesoporous Materials,* vol. 25, pp. 59-74, 1998.

APPENDIX

APPENDIX A – ^{29}Si AND ^{27}Al MAS NMR

Relevant information for the analysis of ^{29}Si MAS NMR can be found below. Figures A2 and A3 represent, respectively, the ^{27}Al and ^{29}Si MAS NMR spectra obtained for the original beta sample, βOS.

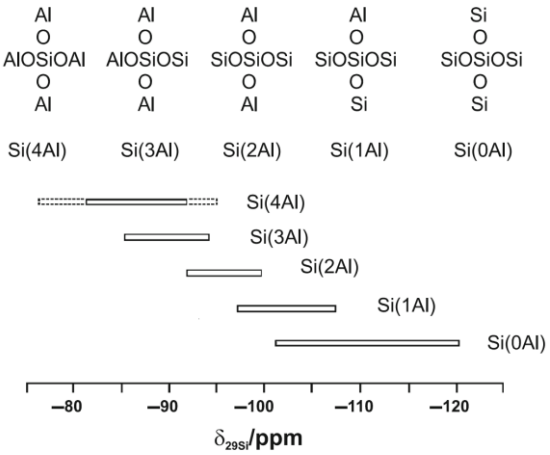

Figure A1 – Typical ^{29}Si chemical shifts for Si(*n*Al) groups in zeolites [43]

The framework Si/Al molar ratio can be calculated according to the following equation [43]:

$$\frac{\mathrm{Si}}{\mathrm{Al}} = \frac{\sum_{n=0}^{4} I_{\mathrm{Si}(n\mathrm{Al})}}{\sum_{n=0}^{4} 0.25 \cdot n \cdot I_{\mathrm{Si}(n\mathrm{Al})}} \qquad \text{(A1)}$$

where *I* is the peak intensity (in red in Figure A3) and *n* is the number of Al atoms surrounding each Si.

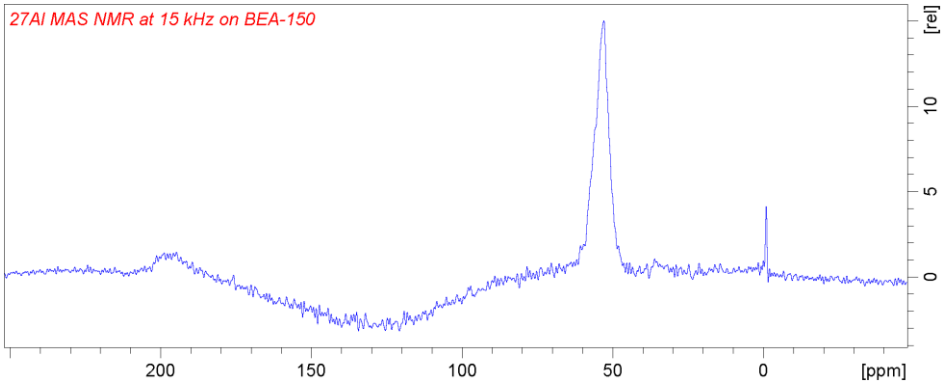

Figure A2 – ^{27}Al MAS NMR spectrum for sample βOS

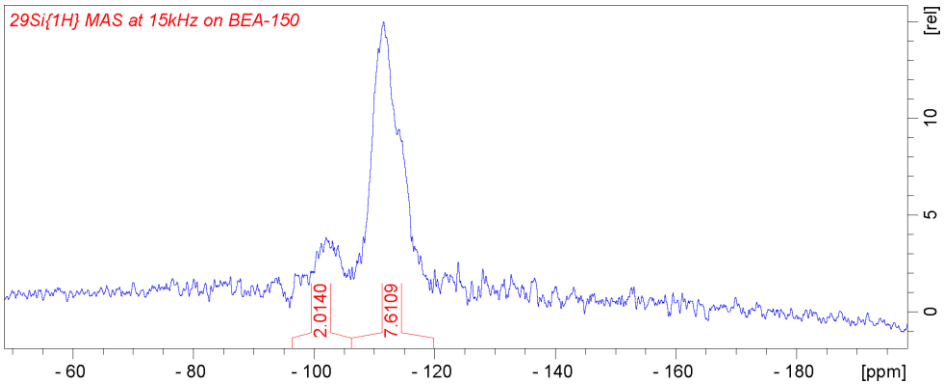

Figure A3 – ^{29}Si MAS NMR spectrum for sample βOS

APPENDIX B – XRD PATTERNS OF ZEOLITE BETA FROM POLYMORPHS A TO B

The following figure represents the different XRD patterns for zeolite beta, from 0% polymorph B (100% BEA in Figure B1) to 100% polymorph B (0% BEA in Figure B1) [44].

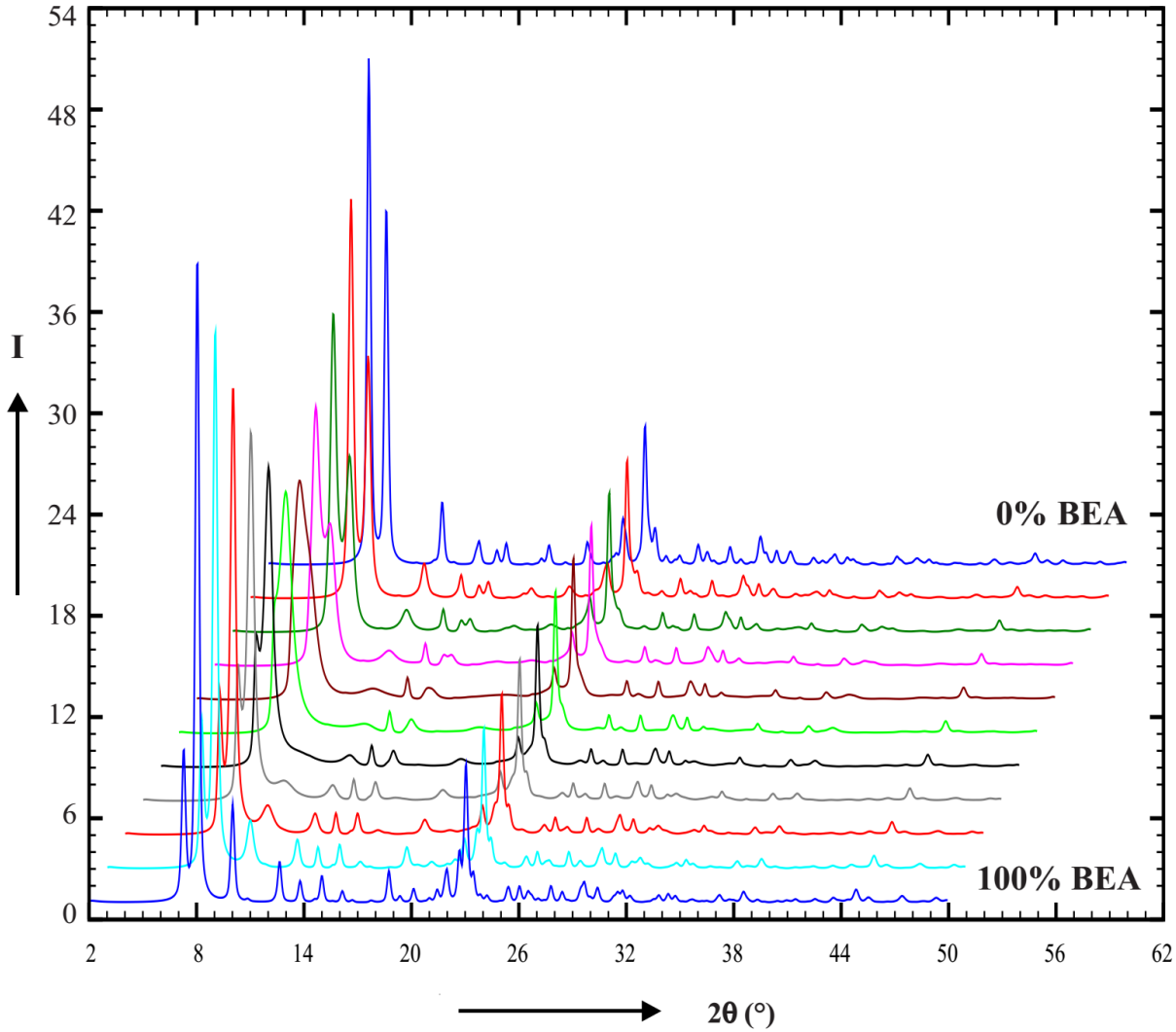

Figure B1 – XRD patterns of zeolite beta from polymorphs A (100% BEA) to B (0% BEA) [44]

APPENDIX C – N_2 SORPTION EXPERIMENTS TABLES

The following tables list the values in the bar charts in Figures 37, 38, 39 and 43.

Table C1 – MultiPoint BET and *t*-plot method (external and micropore) surface area for the uncalcined BEA-150 samples (cf. Figure 37)

Sample	MultiPoint BET surface area (m^2/g)	*t*-method external surface area (m^2/g)	*t*-method micropore surface area (m^2/g)
βOS	519	244	276
βWIKNO$_3$1	508	238	271
βWIKOH2	451	231	220
βWIKOH10	151	114	37
βIEKNO$_3$1	453	209	245
βIEKNO$_3$10	527	246	281
βIEKOH2	403	196	207
βIEKOH10	120	112	9

Table C2 – MultiPoint BET and *t*-plot method (external and micropore) surface area for the calcined BEA-150 samples (cf. Figure 38)

Sample	MultiPoint BET surface area (m^2/g)	*t*-method external surface area (m^2/g)	*t*-method micropore surface area (m^2/g)
βOS, calc.	588	246	342
βWIKNO$_3$1, calc.	595	273	322
βWIKOH2, calc.	526	255	271
βWIKOH10, calc.	38	38	0
βIEKNO$_3$1, calc.	498	245	253
βIEKNO$_3$10, calc.	653	299	354
βIEKOH2, calc.	428	203	225
βIEKOH10, calc.	43	43	0

Table C3 – *t*-plot method micropore volume for the uncalcined and calcined BEA-150 samples (cf. Figure 39)

Sample	*t*-method micropore volume (cm^3/g)	
	Uncalcined	Calcined
βOS	0.115	0.140
βWIKNO$_3$1	0.112	0.133
βWIKOH2	0.092	0.113
βWIKOH10	0.016	0
βIEKNO$_3$1	0.101	0.105
βIEKNO$_3$10	0.117	0.146
βIEKOH2	0.087	0.094
βIEKOH10	0.004	0

Table C4 – DFT pore diameter for the uncalcined and calcined BEA-150 samples (cf. Figure 43)

Sample	DFT pore diameter (Å)	
	Uncalcined	Calcined
βOS	8.2	10.6
βWIKNO$_3$1	8.2	10.2
βWIKOH2	9.8	10.2
βWIKOH10	8.6	67.9
βIEKNO$_3$1	7.8	8.2
βIEKNO$_3$10	8.2	10.2
βIEKOH2	8.2	9.8
βIEKOH10	8.6	101.3